

**Applications of atomic layer deposition and chemical vapor deposition for perovskite solar cells**

Journal:	<i>Energy & Environmental Science</i>
Manuscript ID	EE-REV-02-2020-000385.R2
Article Type:	Review Article
Date Submitted by the Author:	04-May-2020
Complete List of Authors:	Raiford, James; Stanford University, Chemical Engineering Oyakhire, Solomon; Stanford University, Chemical Engineering Bent, Stacey; Stanford University, Department of Chemical Engineering

Applications of atomic layer deposition and chemical vapor deposition for perovskite solar cells

James A. Raiford, Solomon T. Oyakhire, Stacey F. Bent*

Department of Chemical Engineering, Stanford University, Stanford, CA 94305, USA

*Corresponding author: sbent@stanford.edu

Abstract

Metal halide perovskite solar cells (PSCs) have rapidly evolved over the past decade to become a photovoltaic technology on the cusp of commercialization. In the process, numerous fabrication strategies have been explored with the goal of simultaneously optimizing for device efficiency, stability, and scalability. Chemical vapor deposition (CVD) and atomic layer deposition (ALD) have proven to be effective tools for the fabrication of various components of PSCs. This review article examines the application of CVD and ALD for the deposition and modification of charge transport layers, passivation layers, absorber materials, encapsulants, and electrodes. It outlines the use of these vapor deposition techniques in state-of-the-art, multi-junction solar cell devices, and also contains a discussion of the stability of metal halide perovskite materials under CVD and ALD conditions based on *in-situ* characterization reported in literature. This article concludes with insights into future CVD and ALD research directions that could be undertaken to further aid the deployment of PSCs in emerging solar photovoltaic markets.

1. Introduction

Over the course of the past decade, metal halide perovskite solar cells (PSCs) have emerged as an exciting, new thin film photovoltaic (PV) technology. They have garnered a tremendous amount of attention from both the academic research community and solar industry because of their rapid rise in power conversion efficiency (PCE) to over 25% in such a short time span.¹ This outstanding progress is the result of significant advancements in the manufacture of high-quality perovskite absorbers²⁻⁶ and the design of novel contact layers and device architectures.⁷⁻¹¹ It also stems from a better fundamental understanding of the physics that govern the optoelectronic properties of metal halide perovskite materials.¹²⁻¹⁵ Yet, significant strides still need to be made in order for PSCs to become a viable commercial PV technology.¹⁶⁻¹⁸ Further improvements in efficiency will come from optimization of perovskite/contact interfaces and better light management.¹⁹⁻²¹ In addition, the long-term stability of devices must be improved by minimizing internal and external degradation pathways exacerbated by heat and light.²²⁻²⁴ Lastly, the implementation of low-cost and scalable deposition techniques will continue to drive down the cost of PSCs.²⁵⁻²⁷ In the last several years, chemical vapor deposition (CVD) and the related process of atomic layer deposition (ALD) have emerged as valuable fabrication tools to address these future research goals.²⁸⁻³¹

CVD is a technique used to obtain thin solid films by reactions between one or more precursors either in the gas phase or on the surface of a substrate, usually in the presence of some form of reaction initiator – heat, high energy radiation, or plasma. Schematics for two types of CVD processes that have been applied to PSCs are depicted in **Figure 1a**. In one-step deposition, all precursors are introduced into the reaction chamber simultaneously using an inert gas flow (e.g. argon or nitrogen). The species in the gas phase migrate toward the substrate and chemisorb to the surface. Afterwards, they decompose, and by-products are purged out of the reactor. Surface reaction and diffusion of the adsorbed molecules lead to nucleation and formation of each layer of the desired film. Partial decomposition and reaction of the precursors in the gas phase can also occur. In the two-step process, an initial layer of one precursor is first deposited by physical vapor deposition (PVD) (e.g. evaporation), followed by the introduction of a second precursor that reacts with and interdiffuses into the PVD layer. This more non-traditional CVD process is commonly used for the fabrication of perovskite absorber materials and will be discussed further in Section 5.1.

Numerous variations of CVD have been developed to address a wide variety of research and industrial needs. Some of the frequently employed CVD techniques are plasma-enhanced CVD (PECVD), in which the reactions are carried out under high energy plasma to enhance reaction rates at low temperature,³²⁻³⁵ low pressure CVD³⁶⁻³⁹ atmospheric pressure CVD,⁴⁰⁻⁴⁵ and aerosol-assisted CVD (AACVD), in which the precursors are transported in an aerosol to circumvent the need for volatile precursors.⁴⁶⁻⁵⁰ This adaptability

of CVD has made it attractive for large area film depositions, as evidenced by its use in the glass coatings and semiconductor industries.⁵¹ In PSCs, CVD is particularly useful for the design of electrodes, encapsulation layers, charge transport layers, and perovskite absorbers, as shown in **Figure 1c**. Also, the potential for high-throughput CVD methods makes them desirable for the scaled-up production of PSCs.

ALD is a variant of CVD that utilizes a series of successive, self-terminating, and irreversible gas-solid reactions of at least two compounds in a cyclic manner for the deposition of thin, uniform, and conformal films. The typical ALD process proceeds with the sequence depicted in **Figure 1b**. In the first half-reaction, a gaseous precursor is chemisorbed onto the solid surface, and afterwards the by-products and unreacted precursor molecules are purged out of the reactor. In the next half-reaction, a second precursor is pulsed into the reactor where it reacts with available surface sites. All by-products and unreacted precursor molecules are then purged out of the reactor. This cycle is repeated until a film of desired thickness is attained.^{52,53}

The primary advantage of ALD over other deposition techniques is its production of conformal thin films that are independent of substrate structure. This high aspect ratio conformality results from a self-limiting property that restricts each of the ALD half-reactions to no more than one layer of growth.^{54,55} As a result of its precise control at the atomic scale, ALD plays an important role in the synthesis of nanostructures, elucidation and modification of material properties, and fabrication of novel materials, all of which have a broad range of applications in many emerging energy technologies.⁵⁶⁻⁵⁹ Specifically, ALD has proven useful for the design and synthesis of numerous key features in PSCs including hole transport layers, electron transport layers, and passivation layers, all of which are critical to the high performance of PSCs. These numerous uses for ALD in the PSC architecture are illustrated in **Figure 1c**.

In this review, we systematically discuss the applications of ALD and CVD in the fabrication of charge transport layers, passivation layers, electrodes, absorber layers, buffer and interconnecting layers for tandem solar cells, and encapsulants. We also compare ALD and CVD with physical vapor deposition (PVD) techniques used for synthesizing perovskite absorbers. By highlighting the advantages and disadvantages of both sides, we present areas of opportunity for new research into better performing PSCs. Lastly, we include a discussion of mitigation of potential compatibility issues between ALD/CVD processes and sensitive PSC absorbers (Section 8). The examples presented in this review were chosen to illustrate the versatility of ALD and CVD for PSC fabrication and are not meant to be exhaustive. An extensive number of literature reports are summarized in Tables 1 and 2. We also refer the reader to other excellent reviews on ALD and CVD applied to PSCs for additional insights.²⁸⁻³¹

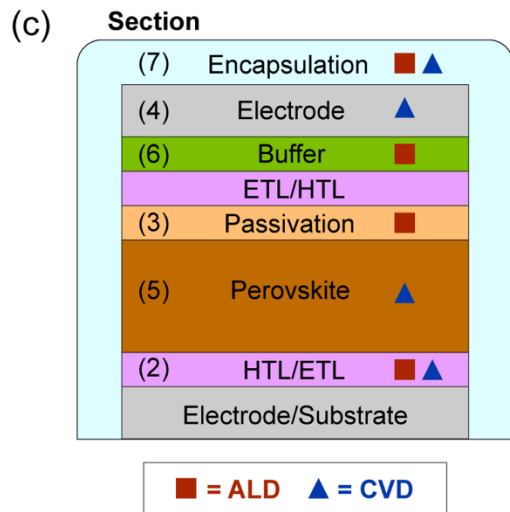
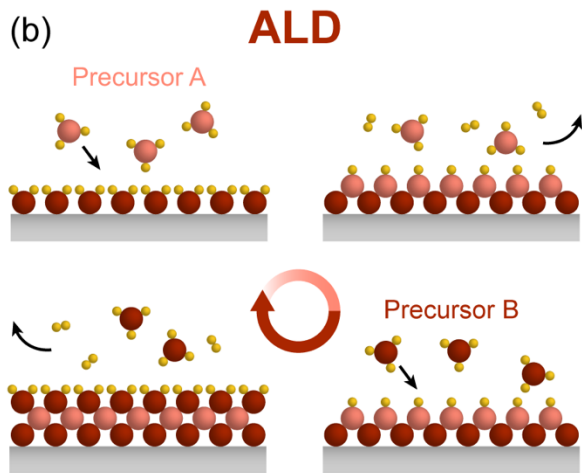
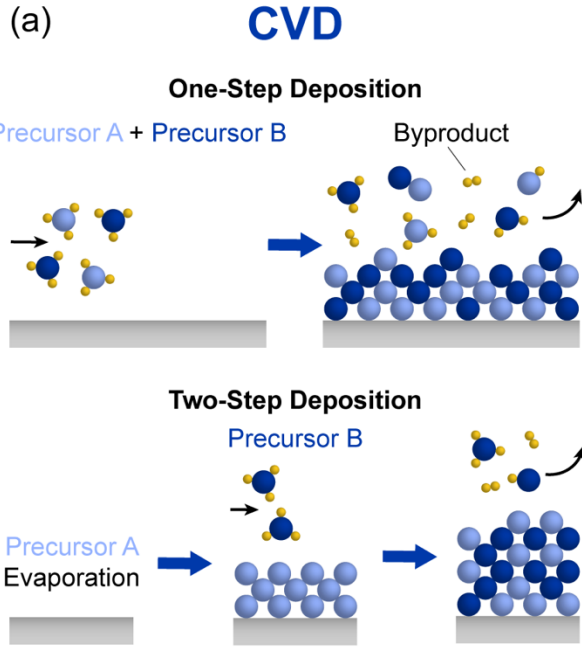


Figure 1: (a) Schematics of two types of two-precursor CVD processing. A one-step deposition entails the simultaneous co-dosing of Precursor A and B into the reactor. In a two-step process, Precursor A is first deposited via evaporation or another physical vapor deposition (PVD) technique. Next, Precursor B is introduced into the reactor, where it reacts with and interdiffuses into the PVD film to form the desired product. (b) Schematic of a single ALD cycle consisting of half-cycles of Precursor A and Precursor B separated by purge steps to remove excess precursor and byproducts. (c) Cross-sectional diagram of a typical PSC highlighting the various components that have been fabricated or modified using ALD and/or CVD. The section numbers for each layer of the device correspond to section numbers in this review article.

2. Charge transport layers

High-quality charge transport layers in PSCs are essential for the efficient collection of photogenerated electrons and holes from the perovskite at their respective electrodes. A good charge transport material should be selective to only one type of carrier through proper energy level alignment with the conduction and valence bands of the perovskite material. It should also be designed to minimize charge recombination, particularly at the perovskite interface. While many techniques have been explored for the design of these layers, ALD and CVD are gaining traction as a result of the high degree of control that they confer over the resulting material properties. In the subsections that follow, we discuss some important examples of where ALD and CVD have been utilized for the synthesis of charge transport layers and highlight the key advantages that each technique holds.

2.1. Electron transport layers

2.1.1. ALD for ETLs

Metal oxides such as TiO_2 ^{60–62} and SnO_2 ^{63,64} have been used extensively as ETLs in PSCs. Borrowing from the dye-sensitized solar cell community, early PSCs adopted a mesostructured configuration. In this design, the perovskite material penetrates inside the framework of a mesoporous ETL, most commonly TiO_2 , on top of a transparent conducting oxide (TCO) electrode. To prevent photogenerated holes in the perovskite from reaching the TCO where they can recombine with electrons, a compact ETL is typically deposited on the TCO first. To be effective, this compact hole-blocking film must be pinhole free. As a result, the method used for the deposition of a compact TiO_2 ETL can drastically influence the overall device performance. Wu et al. demonstrated this effect by fabricating devices with a 50 nm compact TiO_2 ETL using three different deposition techniques: ALD, spray pyrolysis, and spin coating.⁶⁰ The mesostructured solar cells had power conversion efficiencies (PCEs) of 12.56%, 8.76%, and 6.52%, respectively for these three techniques, and the resulting current-voltage (J-V) curves are shown in **Figure 2a**. The authors ascribed the improved performance of the ALD based devices to reduced interfacial charge recombination and lower density of nanoscale pinholes in the compact ETL.⁶⁰

Some disadvantages of single-phase TiO₂ as an ETL for PSCs are that it suffers from a low charge conductivity and high defect density which can limit overall device performance. Several strategies, including doping of the TiO₂, have been explored to address these shortcomings. One novel approach reported by Zhu et al. employed a TiO₂ heterojunction structure for the ETL.⁶⁵ They utilized a combination of ALD and water bath reactions to obtain the anatase and rutile phases of TiO₂, respectively. A heterojunction of the two phases was reported to produce devices with a champion efficiency of 15.3% in comparison to single phase efficiencies of 9.8% and 11.8% for the anatase and rutile phases, respectively. The authors ascribed this significant improvement in PCE to a passivation of trap states, an improvement in carrier extraction, and a reduction in recombination rates that stemmed from improved charge separation of electron-hole pairs at the interface of the heterojunctions.⁶⁵

ALD TiO₂ has also been used as an ETL for inverted, p-i-n devices. In this architecture, the ALD TiO₂ layer not only acts as a selective electron contact but can also help preserve device stability. This device stabilization stems from the dense nature of the TiO₂ film afforded by ALD, preventing moisture from the air from reaching the underlying perovskite absorber. Lv et al. demonstrated a low temperature (60°C) ALD process for producing pinhole free TiO₂ films in planar, inverted devices.⁶⁶ The addition of TiO₂ resulted in a device efficiency of 18.3%, a marked improvement over 16.4% PCE for devices without TiO₂. The ALD TiO₂ also extended the lifetime of cells over the course of several hundred hours of storage in air. This result indicated that the TiO₂ layer not only reduces interfacial charge recombination, but also improves device stability upon exposure to moisture.

Despite the promising devices that have been produced using TiO₂, its inherently low electron mobility and chemical instability under ultraviolet light have motivated the development of more chemically stable and better performing ETLs.⁶⁷ SnO₂ has shown tremendous potential as an ETL in PSCs, in part due to its deep conduction band, high electron bulk mobility ($\sim 240\text{cm}^2\text{V}^{-1}\text{s}^{-1}$), wide optical bandgap (3.6-4.0 eV), and excellent chemical stability.⁶⁴ The effectiveness of an ALD SnO₂ ETL over TiO₂ was first demonstrated by Correa-Baena et al. in planar n-i-p devices.⁶⁸ Band diagrams constructed from ultraviolet photoelectron spectroscopy (UPS) and diffuse reflectance measurements revealed conduction band misalignment between ALD TiO₂ and both MAPbI₃ and MA_{0.15}FA_{0.85}Pb(Br_{0.15}I_{0.85})₃ perovskite that is not present with ALD SnO₂ (**Figure 2b**). The barrier-free alignment for electron extraction from the perovskite to the SnO₂ ETL resulted in hysteresis-free J-V characteristics for devices with a 15 nm ALD SnO₂ ETL grown at 118°C, as shown in **Figure 2c,d**. Furthermore, better charge transport at the SnO₂/perovskite interface led to devices with a PCE as high as 18%. In a similar fashion, Jeong et al. demonstrated that a 12 nm ALD SnO₂ ETL with a 180°C post-deposition anneal also resulted in reproducible devices with a high PCE of 18.3%.⁶⁹

For higher-throughput manufacturing of SnO₂ in the design of PSCs, Hoffmann et al. reported the use of spatial ALD for the synthesis of SnO₂ at atmospheric pressure without a significant reduction in the electrical properties of the ETL.⁷⁰ They documented a champion device efficiency of 12.7% for ETLs deposited at 80°C with a substrate speed as high as 2.4 m/min. The devices also exhibited impressive stability for up to 1000 hours of storage in ambient air and over 3000 hours of storage at 60°C in N₂. Further development of these high-throughput ALD systems will pave the way for roll-to-roll manufacturing of inorganic contact layers in stable PSCs.

For an extensive list of ALD ETLs in PSCs, including their processing conditions and resulting device performances, please refer to **Table 1**.

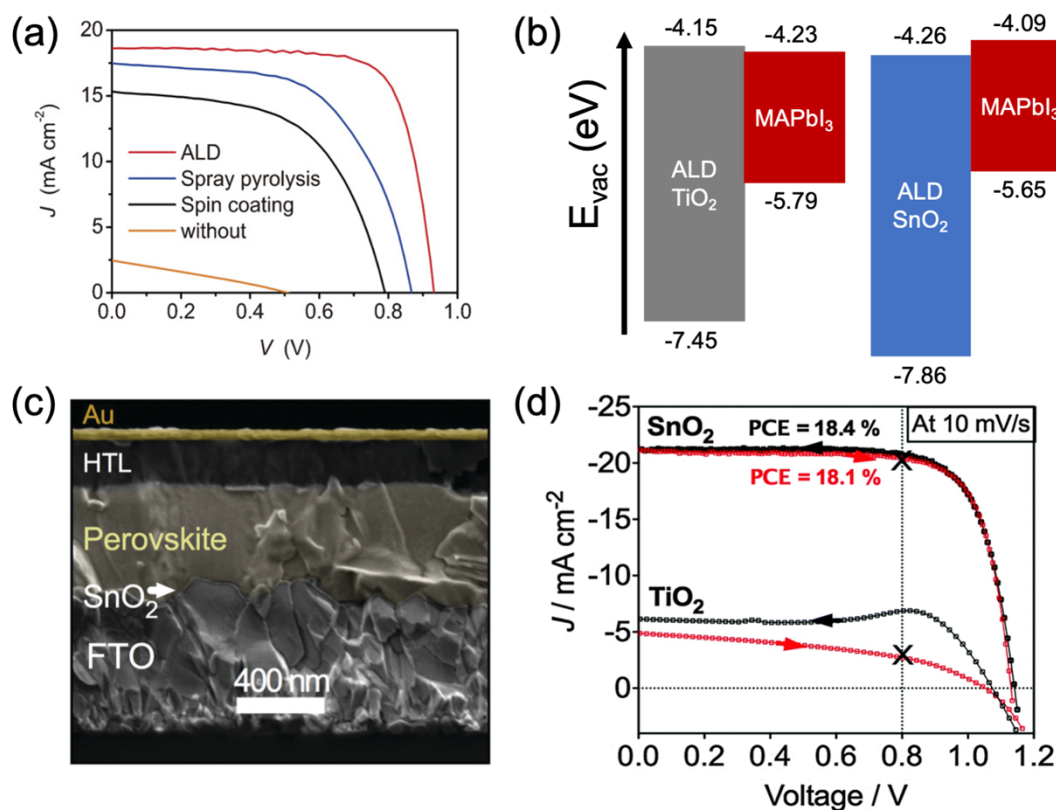


Figure 2: ALD of ETLs in PSCs. (a) J-V curves of PSCs with compact TiO₂ ETLs deposited using different techniques. Reproduced with permission.⁶⁰ Copyright 2014, The Japan Society of Applied Physics. (b) Schematic portraying better conduction band alignment between an ALD SnO₂ ETL and MAPbI₃ compared to an ALD TiO₂ ETL. The two different ALD ETLs were used as substrates for the MAPbI₃ ionization energy measurements. Conduction band and valence band values are with respect to the vacuum level. (c) Cross-sectional scanning electron micrograph (SEM) of a planar n-i-p PSC with an ALD SnO₂ ETL. (d) Forward and reverse scan J-V curves comparing the performance of devices from panel (c) with ALD SnO₂

and ALD TiO_2 ETLs. Reproduced and adapted with permission.⁶⁸ Copyright 2015. Royal Society of Chemistry.

2.1.2. CVD for ETLs

Compared to traditional ALD, CVD growth of ETLs for PSCs can benefit from faster film growth and shorter processing time. The wide array of chemically active electron transport-layer precursors that are available to ALD can equally be utilized in CVD, yet there are limited reports on the use of CVD to synthesize ETLs.^{71,72} Here, we identify a few instances in which CVD has been used for the design of ETLs, and from the reports, draw insights into the factors that have limited CVD-grown ETLs to date.

In an early demonstration of CVD for ETL design, PECVD was reported for the deposition of ZnO nanocolumns with a preferential vertical orientation.⁷¹ However, a champion device efficiency of only 4.8% was achieved with this nanostructured ETL. The authors used electrochemical impedance spectroscopy (EIS) to probe charge transport in the device and found that the low efficiency primarily stemmed from a high carrier recombination rate in the CVD ZnO. As a further demonstration of the use of CVD for the synthesis of ZnO ETLs, Chen et al. designed an AACVD process where 20 nm ZnO was deposited on fluorine doped tin-oxide (FTO) at a temperature of 350°C.⁷³ They reported devices with a PCE of 11.75%, only slightly less than that of ALD-ZnO-based PSCs, which at the time of the report, had PCEs of 13.1%. The authors emphasize the importance of factors such as reaction temperature and precursor concentration on the nucleation and growth of uniform, compact CVD films.⁷³

To circumvent the low-vacuum requirements typically needed for both ALD and CVD processing of thin films, Hodgkinson et al. designed a custom, roll-to-roll atmospheric pressure PECVD process to deposit TiO_{2-x} films for applications as ETLs in PSCs.⁷² They reported the capability of this method to produce sub-50 nm thick films, and demonstrated its ability to outperform similar films grown by sputtering. Drawing from reports around the impact of pinholes in contact layers on device efficiency, we hypothesize that the relatively poor performance of CVD ETLs stems from poor control over the resulting film morphology. Yet we believe that if properly optimized, CVD holds huge promise for high-throughput deposition of ETLs in PSCs. Hence, attention must be placed on the development of processes that balance deposition speed with film quality. With this dual focus, CVD can become more reliable for producing large-area, high-efficiency devices.

2.2. Hole transport layers

2.2.1. ALD for HTLs

NiO is one of the most commonly used inorganic HTL materials for PSCs. It has been shown to possess high transparency, good electron blocking ability, and good valance band level alignment with that of the perovskite.^{74,75} Numerous techniques have been explored for the synthesis of NiO in PSCs, most notably sol-gel processing.⁷⁶ The principal advantage that ALD holds over a sol-gel process is a lower annealing temperature requirement. This key difference makes ALD an attractive, low-energy alternative for NiO deposition. One of the earliest demonstrations of ALD NiO as a high performing HTL in PSCs was carried out by Seo et al.⁷⁷ In p-i-n planar devices, they examined the effect of ALD NiO thickness on device performance (**Figure 3a**). PCE was low (<10%) at higher NiO thicknesses (>10 nm) because the film exhibits bulk insulating properties. At 5 nm, the film thickness becomes comparable to the material's Debye-length, resulting in a higher hole concentration and improved charge transport through the NiO layer. At 2.5 nm, the ALD NiO film is thin enough for electrons to tunnel through, translating to insufficient electron blocking and a reduction in cell efficiencies. To obtain even higher device efficiencies up to 16.4% (open-circuit voltage (V_{oc}) of 1.04 V, short-circuit current density (J_{sc}) of 21.9 mA cm⁻², and fill factor (FF) of 0.72), the authors post-annealed the ALD NiO films at 300°C in order to eliminate water adsorbed to its surface as determined by X-ray photoelectron spectroscopy (XPS). They also connected the removal of water adsorbed to the NiO surface to a reduction in device hysteresis.⁷⁷

To push towards scalable manufacturing of NiO HTLs, Zhao et al. reported a custom-made atmospheric pressure, spatial ALD (AP-SALD) reactor for the deposition of NiO from Ni(CpCH₃)₂ and O₂ at a temperature of 350°C (**Figure 3b**).⁷⁴ The reactor set-up allowed for a deposition rate of 72 cm² nm min⁻¹, and the resultant NiO films were crystalline with a low root-mean-square roughness of 0.6 nm. The authors provided electrical characterization of the NiO as well; the films had a hole concentration of 1.6 x 10¹⁸ cm⁻³, a resistivity of 1.2 x 10³ ohm cm, and a hole mobility of 3 x 10⁻³ cm² V⁻¹ s⁻¹. For devices with 10 nm of the AP-SALD NiO as an HTL, the authors reported a reproducible PCE of 17.1% and FF of >0.8 with negligible hysteresis.⁷⁴

A few other ALD materials have been explored as HTLs in planar PSCs. In a study by Chu et al., an ultra-thin ALD VO_x film grown at 50°C was integrated into p-i-n devices.⁷⁸ The authors reported that UV-treatment of the film led to a maximum device efficiency of 11.5%. Through XPS measurements they found that the UV-treated film had a higher amount of the V⁵⁺ species, corresponding to an increase in the work function of the VO_x and an improvement in the extraction of holes.⁷⁸ ALD VO_x has also been used as a HTL in n-i-p devices.⁷⁹ In this application, the VO_x doubled as a buffer layer on top of the perovskite for

the fabrication of semitransparent PSCs; more details on this system are discussed in Section 6.1. Another promising ALD HTL for PSCs is the alloy formed between TiO_2 and IrO_x . Tan et al. reported the use of ALD for the synthesis of this alloy at 170°C in a p-i-n structured device.⁸⁰ By tuning the cycles ratio of TiO_2 and IrO_x in a supercycle method, they could accurately control the Ir content in the film. Optimal device performance of 15.8% PCE was achieved for a 10 nm thick film with 15.5 mol% IrO_x . This efficiency was higher than the 14.3% PCE reported using sol-gel NiO of identical thickness as an HTL.⁸⁰

For an extensive list of ALD HTLs in PSCs, including their processing conditions and resulting device performances, please refer to **Table 1**.

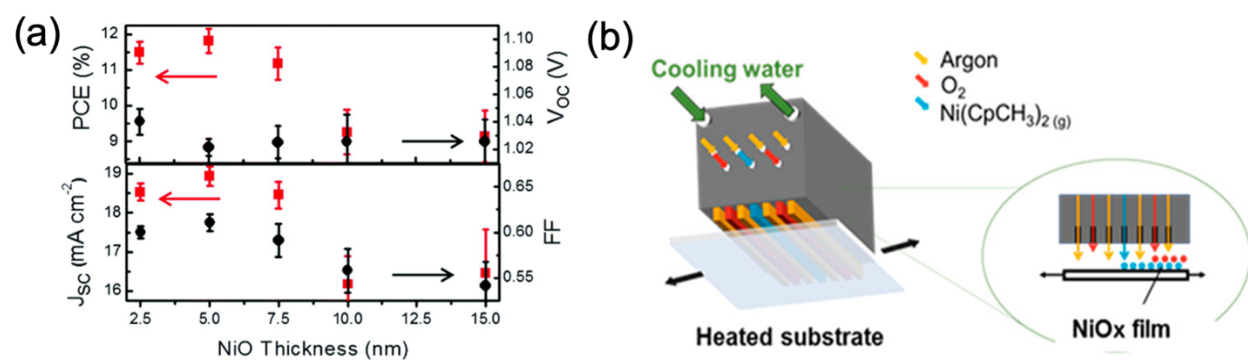


Figure 3: Atomic layer deposition for HTLs in PSCs. (a) PCE and V_{oc} (top) and J_{sc} and FF (bottom) as a function of ALD NiO thickness for planar p-i-n PSCs. Reproduced with permission.⁷⁷ Copyright 2016, The Royal Society of Chemistry. (b) An illustration of an atmospheric pressure, spatial ALD (AP-SALD) reactor system for the growth of NiO films using $\text{Ni}(\text{CpCH}_3)_2$ and O_2 as the precursor and co-reactant, respectively. Reproduced with permission.⁷⁴ Copyright 2018, American Chemical Society.

2.2.2. CVD for HTLs

Like CVD-grown ETLs, there are only a few examples of CVD-grown HTLs applied to PSCs. To the best of our knowledge at the time of this publication, there are no reports of CVD-grown inorganic metal oxides (e.g. NiO) applied in PSCs. Interestingly, there are a few reports around the use of CVD-grown transition metal dichalcogenides (TMDs) as HTLs in PSCs.⁸¹ Here, we highlight the key findings from the use of TMDs in PSCs with a focus on the material properties that make them effective for this application.

TMDs are an exciting class of 2-dimensional (2D) materials that are commonly grown using CVD techniques. The electronic properties of these materials can be tuned through compositional and structural engineering, inspiring researchers to explore their use in optoelectronic devices. One particularly appealing

application of TMDs for PSCs is as carrier-selective contact layers. Recently, Kim et al. reported the CVD growth of MoS₂ and WS₂ as HTLs in p-i-n structured devices.⁸¹ The polycrystalline MoS₂ and WS₂ films were synthesized by thermolysis of (NH₄)₂MoS₄ and (NH₄)₂WS₄ coated silicon substrates, respectively, at 950°C under an H₂/N₂ flow carrying sulfur vapor. Afterwards, the TMDs were removed from the silicon substrates via an etching step and transferred onto the device substrate. Work function values of 4.95 eV and 5.0 eV were measured for the CVD MoS₂ and WS₂, respectively, indicating both 2D materials have good energy level alignment with the valence band of MAPbI_{3-x}Cl_x for efficient hole extraction (**Figure 4a**). Devices fabricated with the MoS₂ HTL were slightly more efficient (9.5% PCE) than those that incorporated the WS₂ HTL (8.0% PCE). Yet, both results were comparable to those of devices with PEDOT:PSS, a common organic HTL, and graphene oxide (GO), another 2D-structured material (**Figure 4b**). While this study highlights the potential for CVD-based TMDs in PSCs, there is still significant opportunity for improvement. For example, the further development of low-temperature processes for growing these 2D TMDs would enable their direct fabrication onto device substrates and eliminate the need for an additional transfer step.

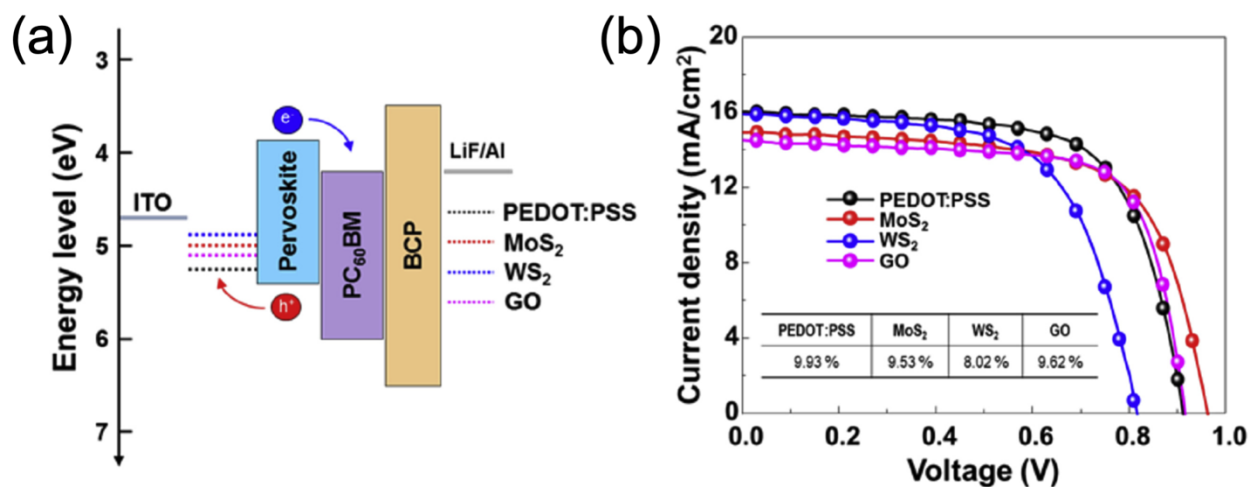


Figure 4: (a) Energy band diagram of a PSC showing the work functions of various HTLs, including 2D MoS₂ and WS₂ grown using CVD. (b) J-V characteristics comparing the performance of PSCs with CVD-grown 2D MoS₂ or WS₂ HTLs to that of devices with PEDOT:PSS or graphene oxide HTLs. Reproduced with permission.⁸¹ Copyright 2016, Elsevier B.V.

3. Passivation layers

Similar to other more established PV technologies, PSC designs often include passivation layers at the perovskite absorber and contact layer interfaces. These passivation layers help to reduce the concentration of surface defects which can lead to unwanted non-radiative carrier recombination at these interfaces. Wide-

band gap metal oxides, such as Al_2O_3 and HfO_2 , are frequently used for passivation layers;^{82–84} however, the insulating nature of these materials dictates that the films be thin enough to allow for the tunneling of charges. This requirement for thin and conformal layers makes ALD and CVD very attractive techniques in the design of passivation strategies for PSCs.

The use of ALD Al_2O_3 is one of the most common passivation strategies for PSCs.^{83,85–90} In one particular example, Koushik et al. demonstrated that ALD half cycles of TMA and H_2O can be used to deposit a thin, uniform Al_2O_3 layer on top of $\text{MAPbI}_{3-x}\text{Cl}_x$ prior to solution processing of a spiro-OMeTAD HTL (**Figure 5a**).⁸⁹ Further details regarding some of the challenges associated with ALD processing directly on the perovskite will be discussed in Section 8. Nonetheless, the authors found that 10 cycles of ALD Al_2O_3 passivation (corresponding to an approximate thickness of 1 nm) improved device PCE from 15% to 18% and reduced the amount of hysteresis observed in the J-V characteristics (**Figure 5b**). In addition to providing a boost in efficiency, the Al_2O_3 layer also stabilized the perovskite films under high humidity conditions (>40% relative humidity (RH)). Devices with the ALD Al_2O_3 maintained 60–70% of their initial efficiency after 70 days of aging, while devices without the Al_2O_3 dropped to just 12% of their initial efficiency. ALD Al_2O_3 passivation between the perovskite and HTL was also reported a couple of years later by Jaysankar et al. for wide-band PSCs. They used alternating cycles of dimethylaluminum isopropoxide (DMAI) and H_2O at 100°C to deposit Al_2O_3 on $\text{Cs}_{0.15}\text{FA}_{0.85}\text{Pb}(\text{I}_{0.71}\text{Br}_{0.29})_3$ ($E_g = 1.72$ eV). Their results indicated that device V_{OC} was strongly dependent on the thicknesses of the passivation layer. The V_{OC} increased by ~ 100 mV up to 1.2 V with 0.8 nm thick Al_2O_3 , then decreased for thicker Al_2O_3 layers. The authors attributed the increase in V_{OC} at low thicknesses to passivation of dangling bonds at the perovskite surface and the drop in V_{OC} at high thicknesses to the dielectric nature of the Al_2O_3 creating a barrier for hole extraction. Lee et al. observed a similar improvement in V_{OC} and overall device efficiency by inserting an ALD Al_2O_3 passivation layer between the compact TiO_2 and mesoporous TiO_2 ETLs of a n-i-p device; they too hypothesized that the improved performance stems from reduced recombination at the ETL interface.⁸³

ALD has been used to grow other metal oxides and nitrides as passivation layers in PSCs, including HfO_2 , ZrO_2 , and TiN .^{82,91,92} Cao et al. introduced an ultra-thin ALD HfO_2 layer between the SnO_2 ETL and indium tin oxide (ITO) electrode of flexible PSCs.⁸² The low temperature (90°C) ALD HfO_2 process was compatible with the flexible polyethylene naphthalate (PEN) substrates and resulted in device efficiencies up to $\sim 19\%$ PCE for an optimized 5 ALD cycles, as shown in **Figure 5c**. An interfacial ALD ZrO_2 layer between MAPbBr_3 and a PC_{61}BM ETL was found to effectively block hole transport and reduce interfacial recombination. Hu et al. used impedance measurements of their devices to extract the carrier recombination

time as a function of photogenerated electron density with and without the ALD ZrO_2 passivation layer, shown in **Figure 5d**.⁹² Over a wide range of illumination levels, the recombination time for electrons was at least an order of magnitude longer with the ALD ZrO_2 passivation, leading to higher photovoltage and photocurrent in devices.

A study by Mali et al. further highlighted the advantage of ALD for conformal passivation with precise thickness control for high aspect ratio surfaces. They designed an ultrathin ALD TiO_2 layer for the passivation of 1D TiO_2 nanorods used as the ETL in mesostructured n-i-p PSC.⁹³ The vertically aligned TiO_2 nanorods were 80-160 nm in diameter and $\sim 2 \mu\text{m}$ in length as measured by SEM. They found that 4.8 nm of ALD TiO_2 was the optimal thickness for the passivation layer, resulting in an average PCE of 13.5% and an average V_{OC} of 0.945 V. These cells were almost twice as efficient as cells with only 2 nm of ALD TiO_2 passivation (average PCE of 7.1% and an average V_{OC} of 0.833). The impact that only a 2-3 nm difference in passivation thickness can have on device performance emphasizes the importance of ALD for those components of a PSC that require atomic-level control.⁹³

For an extensive list of ALD passivation layers in PSCs, including their processing conditions and resulting device performances, please refer to **Table 1**.

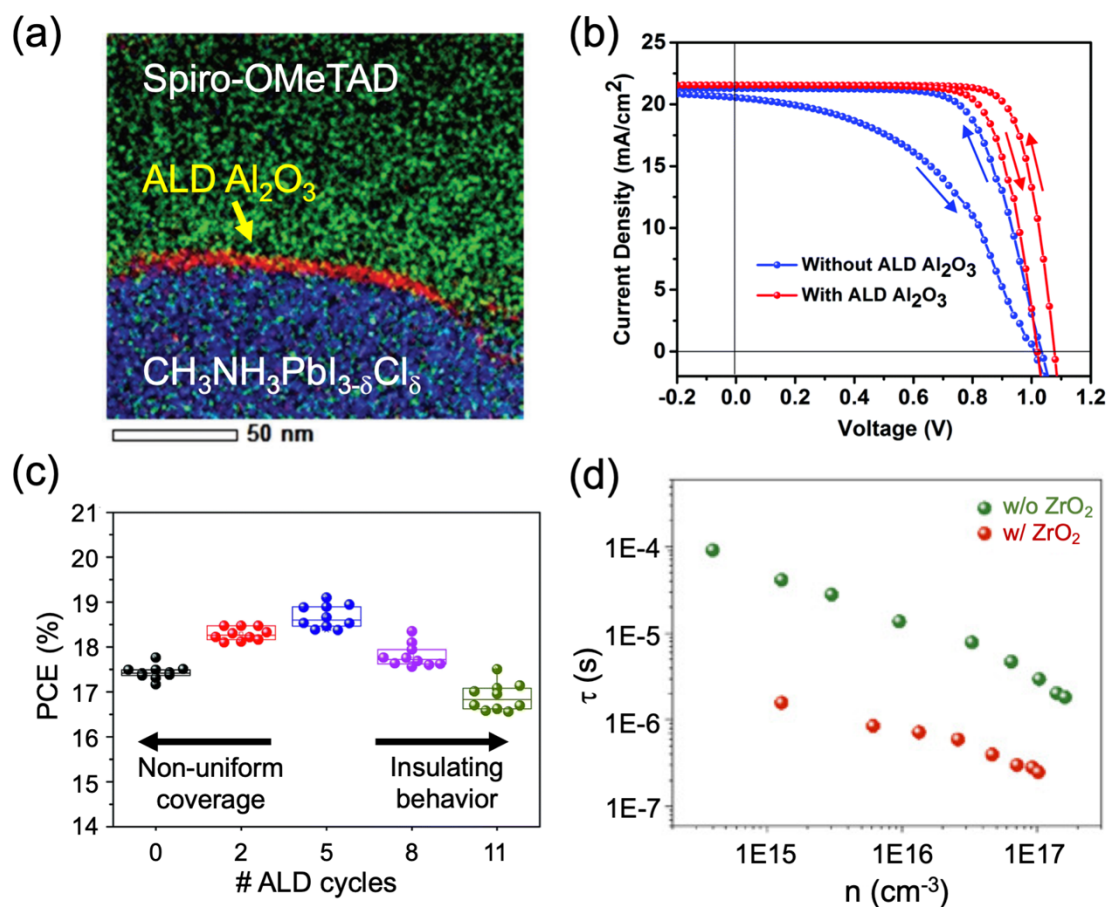


Figure 5: ALD passivation layers in PSCs. (a) Energy dispersive X-ray (EDX) elemental maps of C (green), Al (red), and I (blue) at a perovskite/HTL interface with a conformal ALD Al₂O₃ passivation layer. (b) Forward and reverse J-V scans of PSCs with and without an ALD Al₂O₃ passivation layer on top of the perovskite absorber. Adapted with permission.⁸⁹ Copyright 2017, The Royal Society of Chemistry. (c) Device PCE as a function of the number of ALD HfO₂ cycles deposited as a passivation layer for SnO₂ ETLs. Adapted with permission.⁸² Copyright 2019, The Royal Society of Chemistry. (d) Carrier recombination rates extracted from impedance measurements of PSCs with and without an interfacial ALD ZrO₂ passivation layer between the perovskite and PC₆₁BM ETL. Reproduced with permission.⁹² Copyright 2018, Wiley-VCH.

4. CVD for electrodes

ITO is a common TCO material in the PSC field owing to its transparency in the visible spectrum and high conductivity.⁹⁴ However, the high cost of indium in ITO has motivated the search for a cheaper alternative. Additionally, the brittleness of ITO presents a barrier for its application in flexible devices that are subjected to repeated bending.⁹⁵ Carbon-based electrodes are a potential substitute that address both of these issues. CVD has recently been employed for the growth of 1D-single walled carbon nanotubes and 2D-graphene sheets for application as carbon-based electrodes in both rigid and flexible PSCs.^{96–98} Here, we discuss the

use of these CVD-grown carbon allotropes in the replacement of conventional transparent electrodes for PSCs.

The two-dimensional sheets of sp^2 -coordinated carbon atoms in graphene possess high optical transparency, good conductivity, and excellent mechanical strength, making graphene an attractive replacement for ITO in PSCs.⁹⁹ Sung et al. reported the first PSCs with graphene as the transparent conducting anode by utilizing CVD for the synthesis of the graphene layer.⁹⁷ They adopted a fabrication method reported by Lee et al. in which methane and hydrogen were supplied at 460 mtorr for 30 minutes with the rates of 24 and 8 sccm, respectively, on top of copper foil heated to 1000°C in a quartz tube.¹⁰⁰ The monolayer graphene films were obtained after rapid cooling of the quartz tube to room temperature under H_2 flow. The graphene films were integrated into inverted, p-i-n devices on top of glass substrates, as shown in **Figure 6a**. They introduced an additional MoO_3 layer atop the graphene electrode to improve its wettability for solution processing of subsequent layers in the device and to dope the graphene, reducing its sheet resistance from about 2,000 ohm/cm^2 to 500 ohm/cm^2 (**Figure 6b**). This reduction in sheet resistance led to a significant boost in the device performance from essentially 0% PCE to 17.1% (**Figure 6c**), on par with ITO-based device efficiencies of 18.8%. In addition, the champion devices in the graphene and ITO-based configurations had approximately the same V_{OC} ($\sim 1V$) and J_{SC} ($\sim 22\text{mA}/\text{cm}^2$). Higher series resistance in the doped graphene compared to the ITO electrode was compensated by the fact that the graphene was more transparent resulting in similar photocurrents between the two devices. CVD-grown graphene can also be applied as the top electrode in PSCs using a dry transfer process for the fabrication of semi-transparent devices.¹⁰¹

These ideas can be extended towards the design of flexible PSCs as well.⁹⁶ As shown in **Figure 6d**, they adopted an inverted device configuration in which single layer graphene was transferred onto a thin polyethylene naphthalate (PEN) substrate. Their champion device in this configuration recorded a PCE of 16.8% in comparison to their ITO-based analog which recorded a champion PCE of 17.3%. Nevertheless, they showed that upon introduction of harsh bending conditions (1000 cycles of bending), the graphene-based device retained about 90% of its initial PCE whereas the ITO-based device retained less than 40% of its initial PCE (**Figure 6e**). The authors attributed this improvement to the superior robustness of graphene against mechanical deformation, indicating that it holds high potential in the design of flexible PSCs.⁹⁶ Similar studies corroborate the effectiveness of graphene as a flexible charge conductor and an efficient substitute for ITO in PSCs.^{100,102,103}

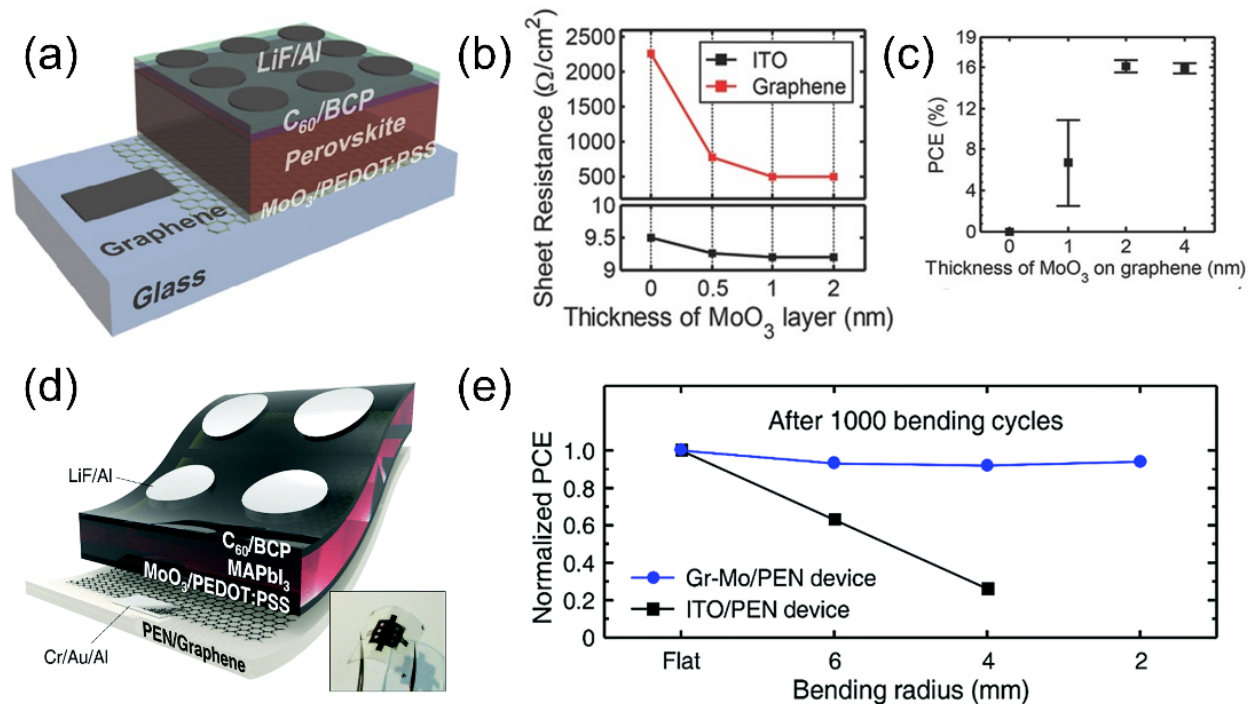


Figure 6: CVD-grown graphene electrodes for PSCs. (a) Schematic of an inverted MAPbI₃ PSC utilizing graphene as a transparent electrode. (b) Relationship between sheet resistance and MoO₃ dopant thickness for graphene-based and ITO transparent electrodes. (c) Relationship between average PCE and MoO₃ dopant thickness for graphene-based transparent electrodes. Reproduced with permission.⁹⁷ Copyright 2015, Wiley-VCH. (d) Device structure of graphene-based flexible PSCs. (e) Normalized PCEs of the graphene and ITO-based devices after 1000 cycles of bending with various radii: flat, 6, 4, and 2 mm. Reproduced with permission.⁹⁶ Copyright 2017, The Royal Society of Chemistry.

Carbon nanotubes, like graphene, also possess good mechanical strength, but their high surface roughness and elevated sheet resistance make it difficult for them to obtain competitive PCEs.^{104,105} In one attempt to demonstrate the applicability of CVD-grown carbon nanotubes in PSCs, Jeon et al. reported the complete replacement of both device electrodes with carbon nanotubes.¹⁰⁶ The scheme for growing the carbon networks involved a floating-catalyst aerosol CVD in which ferrocene vapor was co-introduced with CO into a reactor tube. The ferrocene vapor was decomposed at 880°C into iron nanoparticles that served as catalysts in the subsequent decomposition of CO into carbon nanotubes. With the use of poly(3-hexylthiophene-2,5-diyl) (P3HT) as a p-type dopant and [6,6]-phenyl-C₆₁-butyric acid methyl ester (PC₆₁BM) as an n-type dopant, they reached a maximum device PCE of 7.3%. The authors present a cost-performance trade-off, arguing that despite the relatively low performance of their device, their carbon-based electrodes can reduce materials costs in PSC modules by 66% at scale.¹⁰⁶ In light of these findings,

we believe that for CVD-grown carbon nanotubes to be implemented in a PSC industry, rigorous material optimization must be the guiding principle for subsequent device design.

One overarching theme from most CVD-electrode studies to date is the need for materials or dopants that augment the conductivity of the carbon-based electrodes, indicating that for CVD-grown electrodes to be freestanding, their deposition schemes may need to be modified. Perhaps the development of CVD chemistries that involve the doping of graphene during its formation could alleviate the need for potentially cost-intensive additional processes.

5. Metal halide perovskite absorbers

The absorber layer in PSCs is typically deposited by solution processing techniques, such as spin-coating, due to their ease of fabrication. However, a relative lack of control over solution processing can result in films with large variations in morphology, structure, and porosities.¹⁰⁷ Additionally, there are environmental and health concerns associated with extensive use of organic solvents in solution-based fabrication.^{108,109} A vapor deposition technique like thermal evaporation can generate uniform films on rough or non-uniform surfaces; however, the high financial and energy costs associated with high vacuum equipment makes it difficult to scale-up this technique to large-area devices.¹¹⁰ CVD has the potential to address these problems by enabling conformal deposition that is reproducible over large-area substrates in low-vacuum or atmospheric pressure conditions. In practice, CVD can be utilized for the fabrication of perovskite absorbers through either a two-step or one-step process.^{111–113}

5.1. Two-step CVD

The two-step method first involves the deposition of a metal or metal halide film (e.g. PbI_2) onto a substrate followed by exposure to an ammonium halide vapor (i.e. MAI), converting the film to the desired perovskite phase. A proof-of-concept system for the two-step method was first developed by Leyden et al. for the fabrication of planar MAPbCl_3 devices.¹¹⁴ A schematic of their multi-zone CVD reactor is shown in **Figure 7a**. In the high temperature zone, methylammonium iodide (MAI) was vaporized then transported by a N_2 gas flow to a low temperature zone where it was passed over previously deposited PbCl_2 films on FTO/ TiO_2 substrates. This technique was coined a hybrid CVD (HCVD) process because the MAI precursor started as a solid salt in the reactor. Parameters such as reactor pressure, N_2 flow rate, MAI temperature, and substrate temperature were precisely controlled to ensure high-quality and reproducible perovskite films. Device performance was optimized for an initial PbCl_2 layer thickness of around 100 nm, corresponding to a final perovskite thickness of around 300 nm. In addition, a 120°C post-anneal of the perovskite films in air was found to improve device performance over a post-anneal in an N_2 environment. The maximum PCE achieved in this study was 11.8%, and similar J-V characteristics for an entire batch of devices

showed the relative consistency of the HCVD deposition process. The cells also demonstrated good performance stability after 450+ hours of storage in N₂.¹¹⁴

More recently, a high-efficiency MAPbI₃-based PSC was produced using a similar two-step HCVD design. In this study, Surya et al. first spin-coated PbI₂ onto an FTO/TiO₂ substrate followed by HCVD conversion into MAPbI₃ by way of MAI vapor.¹¹⁵ The authors tuned several parameters, including carrier gas composition, deposition temperature, and post-deposition cooling, to achieve a high-quality perovskite film resulting in a champion PCE of 17.6%. The optimal deposition temperature was found to be 165°C. They reported an optimal carrier gas concentration of 85% N₂ and 15% O₂, proposing that the small amount of oxygen passivated the traps states at the MAPbI₃ surface. Also, their report stated a reduction in shunting pathways when the post-deposition cooling rate was lowered to 0.7°C/min, indicating desirable crystallization rates for MAPbI₃ and a reduction in the concentration of pinholes. As a final parameter, they discovered relative improvements over planar devices when a mesoporous TiO₂ scaffold was used. This improvement was attributed to better crystallinity of the mesoporous TiO₂-based MAPbI₃ films as shown by the XRD spectra in **Figure 7b**. Forward and reverse J-V scans of the champion two-step HCVD MAPbI₃ device are shown in **Figure 7c**, exhibiting negligible hysteretic behavior.¹¹⁵

Luo et al. proposed a slightly different reactor design for two-step CVD synthesis of MAPbI₃ absorbers. In their *in-situ* tubular CVD (ITCVD) reactor, PbI₂ films were placed directly above the MAI powder source in a single temperature zone heated to 145°C and allowed to react for 120 minutes.¹¹² The films formed during the deposition were washed in isopropanol and annealed in air at 145°C for 30 minutes before finishing the device structure. MAPbI₃ films were deposited on substrate sizes up to 4 cm x 4 cm, demonstrating the potential scalability of the technique. Subsequently, the authors attributed the good optical properties of the absorber to its high crystallinity and verified its crystal structure using XRD. With a champion device efficiency of 12.2%, they indicated that their technique holds high potential for future mass production of perovskites.¹¹² Other reports of two-step HCVD processes for the fabrication of MAPbI₃ devices have also been published.¹¹⁶ In addition, more complex perovskite stoichiometries have been reported using this method; for example, Sn/Pb alloys with various atomic ratios of the two metals can be converted to low band gap ($E_g < 1.4$ eV) perovskite films.¹¹⁷ While two-step CVD shows promise for the fabrication of high-quality perovskite absorbers, a desire to minimize the number of processing steps associated with perovskite deposition has also led researchers to explore one-step CVD schemes.

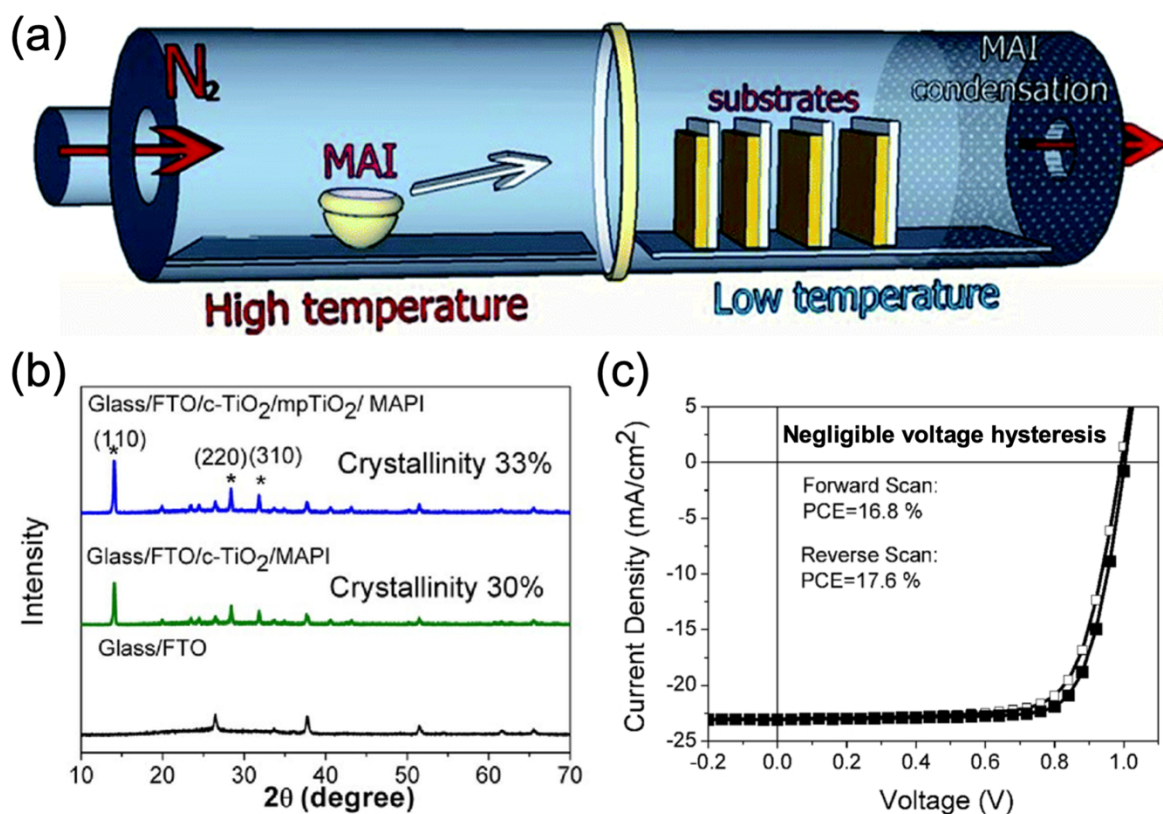


Figure 7: Two step CVD for perovskite absorber synthesis. (a) Schematic of a hybrid CVD (HCVD) furnace for MAI deposition. Adapted with permission.¹¹⁴ Copyright 2014, The Royal Society of Chemistry. (b) X-ray diffraction (XRD) spectra of MAPbI₃ films deposited by HCVD on both compact and mesoporous TiO₂ substrates. (c) J-V characteristics of an optimized, HCVD-based MAPbI₃ device on a mesoporous TiO₂ ETL. Reproduced with permission.¹¹⁵ Copyright 2018, Society of Photo-Optical Instrumentation Engineers.

5.2. One-step CVD

In one-step CVD, the perovskite is synthesized by a single reaction of the precursor vapors in the gas phase before subsequent deposition onto the substrate. This method provides a direct route to the synthesis of perovskites with a focus on fewer control parameters, unlike the two-step CVD method. Tavakoli et al. designed a one-step CVD furnace for the synthesis of MAPbI₃ and MAPbI_{3-x}Cl_x absorbers by co-vaporizing MAI and PbX₂ (X = I or Cl) salts under an argon gas flow at 360°C (**Figure 8a**), resulting in device PCEs as high as 11.1%.¹¹⁸ Scanning electron microscopy images of the CVD MAPbI_{3-x}Cl_x films showed large perovskite morphological grain sizes with good surface coverage, and time-resolved photoluminescence measurements indicated long carrier lifetimes (~120 ns) and diffusion lengths (700-800 nm), which are important for maximizing the collection of photogenerated electrons and holes from the perovskite layer.¹¹⁸

Another strategy for one-step CVD of perovskite absorbers is to use an AACVD approach. In an AACVD design, the perovskite precursor salts are first dissolved in solvent. An ultrasonic nebulizer is then used to aerosolize the precursor solution before it is carried by an inert gas flow into the reactor to react with the heated substrates. The ability to carry out this one-step reaction process at atmospheric pressure is attractive for scaled-up fabrication. AACVD of MAPbBr_3 was first demonstrated by Lewis et al. in 2014 (**Figure 8b**).¹¹⁹ Shortly after, Bhachu et al. reported the use of AACVD to grow phase pure and compositionally uniform MAPbI_3 films at 200°C.¹²⁰ Later studies on one-step AACVD further examined the effects of various processing parameters on the nucleation and growth of the perovskite absorbers. Afzaal et al. found that the position of the substrates in a hot wall reactor was critical for obtaining uniform, high-quality MAPbI_3 films. If the substrates were placed too far from the precursor vapor inlet, the conversion of PbI_2 to perovskite was limited by mass diffusion of MAI to the substrate surface. Additionally, the authors optimized the structure and morphology of AACVD MAPbI_3 with respect to the reaction temperature. At the optimal temperature of 250°C, the resulting perovskite layer was a highly crystalline and compact film.¹²¹ Lastly, Basak et al. investigated the effects of varying the halide composition of the $\text{MAPbI}_{3-y}\text{Br}_y$ precursor solution on the resultant film properties. For a deposition temperature of 140°C, they found that the perovskite morphological grain size increased with increasing bromine content (**Figure 8c**), yet energy-dispersive X-ray (EDX) spectroscopy revealed that in all cases, the films were still iodine rich relative to the stoichiometry of the starting precursor solution.

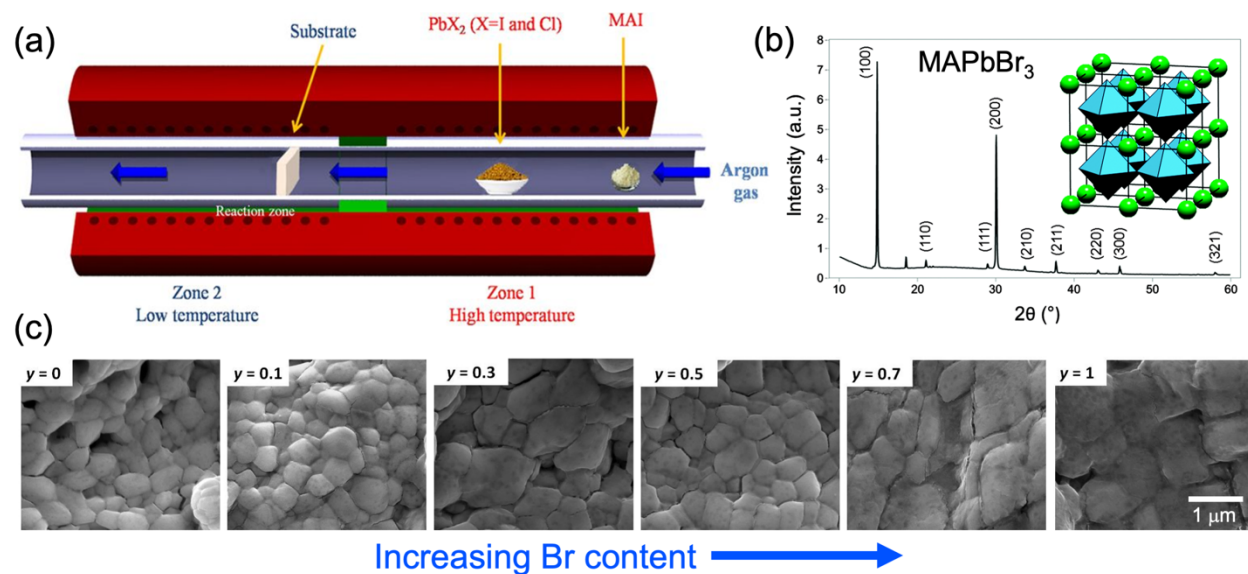


Figure 8: CVD for one-step synthesis of perovskite absorbers: (a) Schematic diagram of a one-step CVD furnace with co-evaporation of MAI and PbX_2 ($X = \text{I}$ or Cl) precursors in a high temperature zone upstream of the substrate. Reproduced with permission.¹¹⁸ Copyright 2015, Springer Nature. (b) XRD spectrum of a MAPbBr_3 film deposited by AACVD at 250°C . The inset shows the perovskite crystal structure with green MA^+ cations surrounded by blue PbBr_6 octahedra. Adapted with permission.¹¹⁹ Copyright 2014, The Royal Society of Chemistry. (c) SEM images of the top surfaces of $\text{MAPbI}_{3-y}\text{Br}_y$ films deposited by AACVD with increasing amounts of bromine content. Adapted with permission.¹¹³ Copyright 2019, Elsevier B.V.

5.3 ALD proofs-of-concept

To date, ALD has not been used in practice for the deposition of the perovskite absorber layer in PSCs. The slower deposition rates associated with the sequential nature of ALD reactions would necessitate prohibitively long deposition times for perovskite films with thicknesses on the order of hundreds of nanometers. Nevertheless, two recent studies reported the use of ALD to grow a precursor seed layer that can then be converted to MAPbI_3 in a post-treatment step. Sutherland et al. started with ALD of PbS from alternating pulses of lead(II) bis(2,2,6,6-tetramethyl-3,5-heptanedionate) ($\text{Pb}(\text{tmhd})_2$) and H_2S at 150°C . They then vapor treated the PbS films in iodine gas to form PbI_2 followed by conversion to MAPbI_3 in a MAI solution.¹²² Popov et al. reduced the number of conversions by using ALD to grow the PbI_2 directly. The PbI_2 was deposited using alternative half-cycles of lead(II) bis(bis-(trimethylsilyl)amide) ($\text{Pb}(\text{btsa})_2$) and tin(IV) iodide (SnI_4) in a temperature window of $70\text{--}90^\circ\text{C}$. A single vapor treatment step with MAI converted the ALD PbI_2 to MAPbI_3 . While there have been no reports of devices incorporating ALD-based perovskite absorbers, these two studies serve as proofs-of-concept for future development of a metal halide perovskite ALD processes.

5.4 Comparison of CVD and ALD with other vapor deposition methods used for PSC absorbers

Besides CVD, various other vapor deposition techniques such as PVD have been successfully applied towards the fabrication of absorbers in PSCs.^{123,124} One commonly used PVD method is multi-source thermal evaporation, in which the perovskite precursors are independently and simultaneously heated to their sublimation temperatures and co-deposited on a substrate suspended overhead.^{125,126} Similar to the one-step CVD method, it can be challenging to control perovskite film stoichiometry or access more complex perovskite compositions using this technique. This difficulty arises from differences in sublimation temperatures and partial pressures of metal halide and organic cation precursors, making it difficult to control individual precursor deposition rates.¹²⁷ In addition, the requirement for each precursor powder to have its own source increases the design complexity of tools needed for the deposition of multi-component films. These limitations are particularly relevant given that many recent advances in device stability and multi-junction PSCs rely on carefully tuning the ratios of several different cations (e.g.

methylammonium, formamidinium, cesium, etc.), metals (e.g. tin and lead), and halides (e.g. iodide, bromide, and chloride).^{3,4,128,129} Two-step CVD, sequential vapor deposition of precursors, or post-treatments can offer more flexibility in terms of achieving multi-component perovskite films, but often require multiple fabrication steps or tools, making them less financially attractive for scaled-up device fabrication.^{117,130,131} Single-source and flash evaporation techniques, in which a pre-formed perovskite film or powder is rapidly evaporated from a single-source heater, has also been implemented with some success.^{132,133}

There are some key differences between CVD/ALD schemes and the PVD techniques mentioned thus far that are important to consider with regard to large-scale perovskite absorber fabrication. PVD systems, which typically operate at pressures between 10^{-5} to 10^{-7} torr, have higher vacuum requirements than their CVD counterparts. Not only do these high vacuum conditions add costs associated with pumping equipment, but they also limit PVD to batch processing. On the other hand, CVD reactors, which operate from low vacuum (10^{-3} torr) to atmospheric pressure, are much more amenable to roll-to-roll processing, leading to higher throughput manufacture of perovskite films.⁷² Another important factor to consider is the amount of precursor material used per device area. In large PVD chambers, there is typically a large distance between the source and substrate, leading to a significant amount of wasted precursor material being deposited on the chamber walls. To counteract this issue, close-proximity ALD and CVD reactors have been engineered to shorten the distance between precursor inlets and the substrate. By using inert gas curtains to separate precursor zones, these types of reactors enable precursor recycling which can greatly reduce materials waste. To date, close-proximity reactors have mostly been used for metal oxide growth,^{70,72,74} yet the design could be extended to the growth of perovskite absorbers as well. While vacuum-based PVD systems have been successfully adopted in other mature semiconductor and coatings industries, continuous CVD processing in an atmospheric pressure reactor is an exciting alternative prospect for the fabrication of metal halide perovskite films.

6. ALD and CVD for tandem solar cells

Improvements in the PCE of a given solar cell technology directly correlate to reductions in the overall PV system cost. Tandem solar cells are a proven strategy for achieving higher PCEs beyond the Shockley-Queisser limit for single-junction cells.¹³⁴ Due to their tunable band gap and low-cost deposition methods, metal halide perovskites are uniquely suited for tandem solar cell applications.^{135–139} Lead-based perovskites have been utilized as the wide band gap subcell of tandem devices in conjunction with a low band gap absorber, such as crystalline silicon^{140–147} or copper indium gallium selenide (CIGSe).¹⁴⁸ Wide band gap and low band gap (achieved by alloying Sn with Pb at the metal site) perovskites can also be used

together in all-perovskite tandem devices.^{128,149–153} In the past several years, ALD metal oxide layers have significantly contributed to the development and success of perovskite tandems, which are now approaching PCEs of 30% at the laboratory scale. In this section, we will discuss the various uses and benefits afforded by ALD for perovskite tandems.

6.1. Buffer overlayers

Tandem devices require that the wide band gap subcell be semitransparent, allowing near-infrared (NIR) light to pass through and be absorbed in the low band gap subcell. This condition dictates that both electrodes of the wide band gap cell in a 4-terminal configuration, or the front electrode and interconnecting layer in a 2-terminal configuration, be highly transmissive. TCOs are frequently used for these applications and are often sputtered on top of the perovskite subcell. To avoid damage to the perovskite material during sputtering, an additional buffer layer is employed.

The most common example of an ALD buffer overlayer is the use of SnO₂ in the p-i-n architecture. ALD SnO₂ was first demonstrated in this capacity by Eperon et al. for all-perovskite tandems and by Bush et al. for 2-terminal perovskite-silicon tandems (**Figure 9a**).^{140,149} Since then, many of the highest-reported efficiency (some >25%) perovskite tandem solar cells utilize an ALD SnO₂ buffer overlayer.^{128,141,142,144,150,154,155} These SnO₂ layers are typically grown at low temperatures (<120°C) using TDMASn and water as the metal-organic precursor and co-reactant, respectively. While the SnO₂ itself is an electron-selective transport material, an additional fullerene layer is deposited prior to ALD processing. Issues associated with ALD processing directly on the perovskite material will be covered in Section 8. In addition to its role as a sputter buffer layer, the ALD SnO₂ also improves the long-term stability of the perovskite cell (**Figure 9a**). Water and oxygen ingress from the air, metal diffusion from the electrodes, and the evolution of volatile decomposition products at elevated temperature are all degradation pathways that limit the stability of perovskite solar cells. The dense and conformal nature of an ALD metal oxide layer helps minimize the extent to which these processes occur.

Our group recently demonstrated that ALD vanadium oxide (VO_x) can also be used as a sputter buffer overlayer in the n-i-p architecture.⁷⁹ Previously, thermally evaporated molybdenum oxide (MoO_x) has been commonly used in this capacity; however, MoO_x has been shown to interact negatively with the perovskite material leading to device failure.^{156,157} Preliminary long-term stability tests with the VO_x were promising, with devices maintaining their performance after 1000 hours at 85°C in N₂.⁷⁹

6.2. Contacts for non-planar tandems

A low band gap subcell with a rough or textured surface presents additional constraints for the subsequent processing of a perovskite subcell in a 2-terminal tandem configuration. Mainly, each layer in the perovskite subcell must conformally coat surface features ranging from the nanoscale to microscale without pinholes or large defects that could short the device. Solution deposition techniques such as spin coating or blade coating can be ineffective in these applications, particularly for contact layers which tend to be only tens of nanometers thick. Instead, one can take advantage of the self-limiting, gas phase reactions of ALD to achieve conformal deposition of ultra-thin contact layers in non-planar devices. One excellent example of this application of ALD was recently published by Jošt et al. for a perovskite-CIGSe tandem cell.¹⁴⁸ Multi-stage evaporation of the CIGSe absorber layer resulted in a rough surface morphology of the bottom cell with feature sizes ranging from 50 nm to 1 μm . To avoid shunting of the perovskite subcell, the authors utilized a 10 nm layer of ALD NiO_x grown at 150°C as the hole contact layer. Conformal growth of the ALD NiO was confirmed by EDX mapping of transmission electron microscopy (TEM) images (**Figure 9b**). They also employed a SnO_2 buffer layer on top of the perovskite to enable the deposition of an indium-doped zinc oxide transparent electrode, as discussed in section 6.1.

Another example of ALD for contact layers in non-planar tandem devices was reported by Sahli et al. in the first demonstration of a fully textured perovskite-silicon tandem solar cell.¹⁴⁴ Up until then, 2-terminal perovskite-silicon tandem devices featured silicon subcells with polished front surfaces to allow for solution deposition of the perovskite cell on top. Most commercial silicon cells are made with texturing on both sides to minimize surface reflection through light trapping. Polishing one side of the cell introduces an additional costly step to the fabrication process and results in undesirable reflections that limit photocurrent. Sahli et al. designed a fully vapor-processed perovskite cell to preserve the texturing of the underlying silicon cell and relied upon the conformality of an ALD SnO_2 buffer layer (described in section 6.1) to complete the front electrode, resulting in an impressive tandem cell efficiency of 25.2%.¹⁴⁴

6.3. Recombination layers/tunnel junctions

Another important component of 2-terminal tandem devices is the interlayer that connects the two subcells in series. Ideally, this interlayer should efficiently shuttle photogenerated carriers between the two subcells with minimal electrical and optical losses. One common approach is to use a TCO, such as ITO, indium zinc oxide (IZO), or aluminum-doped zinc oxide (AZO), as a recombination contact. In an early demonstration of this strategy, Albrecht et. al. utilized ALD SnO_2 (15 nm) together with sputtered ITO (80 nm) to form a recombination contact in monolithic, n-i-p perovskite-Si tandem solar cells, resulting in a stabilized power output (SPO) efficiency of 18.1%.¹⁵⁸ The use of a thick TCO as a recombination layer,

however, can result in significant parasitic absorption of visible and near-infrared light that limits the achievable photocurrent in the low band gap subcell. Additionally, high lateral conductivity of the sputtered TCO can exacerbate shunt pathways in either subcell. To address both of these issues, Palmstrom et al. developed a thin, 25 nm recombination layer of ALD AZO for all-perovskite, 2-terminal tandem solar cells.¹²⁸ The conformal ALD TCO recombination layer sufficiently protected the bottom cell during subsequent fabrication of the top cell. The ALD AZO also had a high sheet resistance, preventing lateral conduction of carriers to shunt pathways, but was thin enough to not impede out-of-plane carrier transport between subcells. This tailored ALD recombination layer enabled the fabrication of both rigid and flexible 2-terminal, all-perovskite tandem solar cells with PCEs of 23.1% and 21.3%, respectively, as shown in **Figure 9c**.

Instead of a single recombination layer, some monolithic, multi-junction solar cells use tunnel junctions as interconnects. In a typical p-n tunnel junction, a narrow depletion region forms at the interface between heavily doped p-type (p^+) and n-type (n^+) materials, allowing carriers to tunnel between subcells with low electrical resistance and a minimal loss in voltage. For example, some perovskite-Si tandem devices intentionally add tunnel junctions consisting of adjacent p^+ and n^+ doped, hydrogenated amorphous or nanocrystalline silicon deposited by PECVD.^{144,159,160} However, adding layers to the device stack to create a tunnel junction can also introduce unwanted parasitic absorption and limit tandem efficiency. To avoid this problem, Shen et al. engineered the interface between the p^+ emitter of a silicon homojunction bottom cell and the ALD TiO_2 ETL of a perovskite top cell to directly contact the two subcells without adding an n^+ doped interlayer.¹⁴⁶ The *in-situ* tunnel junction between the ALD TiO_2 and p^+ silicon produced a highly ohmic contact with low resistive losses and minimal optical absorption. Consequently, the resulting tandem solar cell had an SPO efficiency of 24.1%, a marked improvement over previous 2-terminal perovskite-Si tandems in the n-i-p architecture.

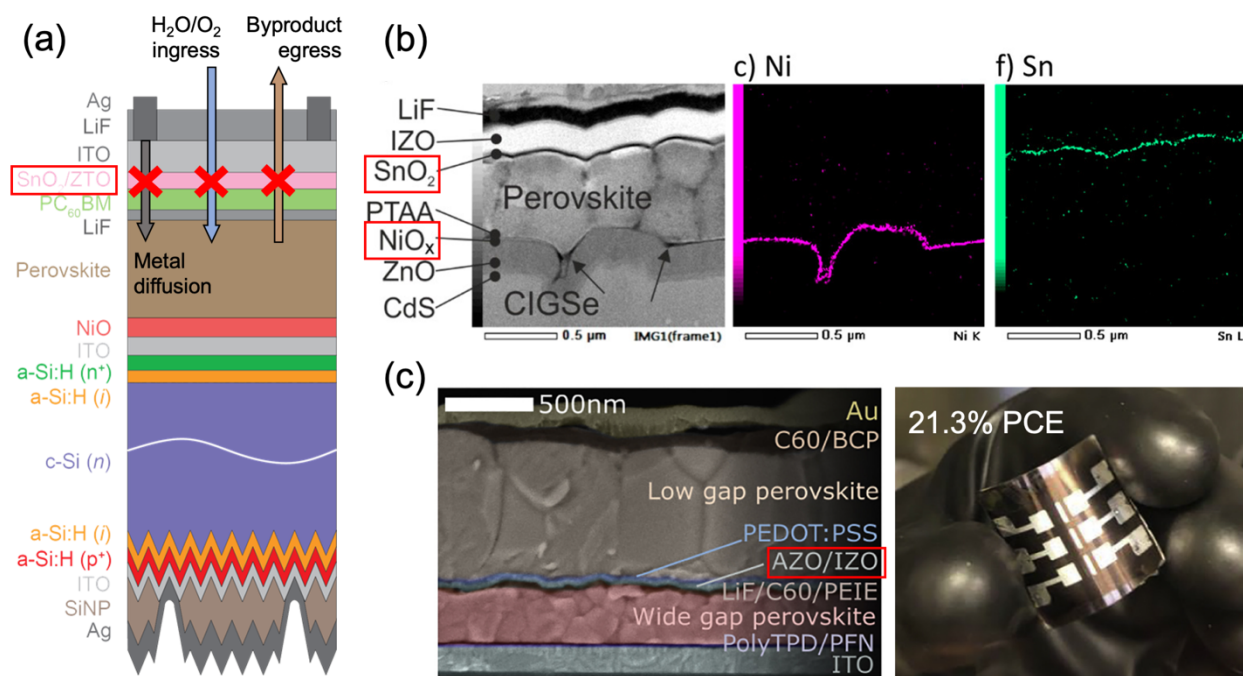


Figure 9: In each panel, the ALD layers are highlighted by red boxes. (a) Cross-sectional schematic of a perovskite and heterojunction silicon tandem solar cell with an ALD SnO₂/ZTO buffer overlayer. The ALD buffer overlayer helps to block various degradation pathways (indicated by arrows), improving the long-term, operation stability of the device. Reproduced and adapted with permission.¹⁴⁰ Copyright 2017, Springer Nature Publishing AG. (b) High-angle annular dark-field scanning transmission electron microscopy (HAADF-STEM) cross-section of a monolithic perovskite-CIGSe tandem solar cell. Elemental maps from energy-dispersive X-ray (EDX) spectroscopy show conformal deposition of ALD NiO and SnO₂ within the tandem structure. Reproduced with permission.¹⁴⁸ Copyright 2019, American Chemical Society (c) Cross-sectional scanning electron micrograph (SEM) of an all-perovskite tandem solar cell with an ALD AZO recombination layer. A photograph of a flexible all-perovskite tandem device with a stabilized PCE of 21.3% is also shown. Reproduced with permission.¹²⁸ Copyright 2019, Elsevier Inc.

7. Encapsulation

In order for perovskite solar cells to become a viable, commercial PV technology, they will ultimately need to demonstrate stable operation in the field over the course several years to decades. While developing strategies to minimize internal degradation pathways within the solar cell is imperative to achieving this goal, external encapsulation of the cells to isolate them from stressors in the environment, such as oxygen or moisture, is equally as important. For rigid modules, the perovskite solar cell community can largely mimic the glass encapsulation designs used by the well-established silicon PV industry. Many emerging applications of solar PV, however, could benefit from light-weight, flexible perovskite modules. For flexible perovskite devices, the encapsulants themselves must also be flexible. In addition, they should be impermeable to moisture and resilient against fracture or delamination upon repeated bending or flexing.

Thin film encapsulation (TFE) is one promising candidate for enabling the long-term environmental stability of flexible perovskite devices. TFE typically consists of a dense inorganic layer with a low water vapor transmission rate (WVTR), a nanolaminate of alternating organic and inorganic layers, or a hybrid organic-inorganic material.¹⁶¹ The addition of organic interlayers provides additional flexibility and can even further reduce the WVTR. ALD and CVD are both attractive techniques for the deposition of TFE materials and are used commercially for the encapsulation of organic electronics and light-emitting diodes (LEDs). While CVD is currently more prevalent in industry due to its high-throughput processing, ALD has garnered significant attention for TFE because of the high-quality films that it affords.¹⁶¹

To date, there have been a limited number of reports of ALD or CVD for TFE of perovskite solar cells. A short summary of the results from each study is listed in **Table 2**. The simplest designs focus on the use of a single layer of ALD Al₂O₃ to protect devices from moisture in the air. Choi et al. demonstrated that 50 nm of ALD Al₂O₃ deposited using TMA and water at 95°C can stabilize mesoporous FA_{0.85}MA_{0.15}Pb(I_{0.85}Br_{0.15})₃ devices in humid conditions.¹⁶² They reported only a 4% drop in PCE following 7500 hours (~10 months) of storage at room temperature in the dark with 50% RH. Ramos et al. highlighted the importance of using a low-temperature TFE deposition process for perovskite applications.¹⁶³ By reducing the ALD Al₂O₃ deposition temperature from 90°C to 60°C, they were able to retain a higher initial PCE following encapsulation, as shown in **Figure 10a**. The low-temperature encapsulation process also improved device longevity. MAPbI₃ solar cells coated with 16 nm of ALD Al₂O₃ retained >75% of their initial efficiency upon aging in ambient air for 2256 hours.

Integrating organic layers with inorganic materials is one strategy to improve the efficacy and/or flexibility of TFEs. In one of the first demonstrations of TFE for PSCs, Chang et al. encapsulated semitransparent MAPbI₃ devices with a PET substrate coated in 50 nm of ALD Al₂O₃ (**Figure 10b**).¹⁶⁴ Not only did the bilayer encapsulant result in devices with minimal PCE loss after 45 days of storage in ambient air, but it also maintained low ambient WVTRs of 2.1 x 10⁻³ g m⁻² day⁻¹ and 7.9 x 10⁻³ g m⁻² day⁻¹ following 1000 bending cycles at a bending radius of 13 mm and 5 mm, respectively. Choi et al. reported a similar design using a bilayer of polydimethylsiloxane (PDMS) (55 μm) and ALD Al₂O₃ (30 nm) on top of FA_{0.85}MA_{0.15}Pb(I_{0.85}Br_{0.15})₃ devices.¹⁶⁵ The authors showed that ALD Al₂O₃ permeates into the PDMS film, filling voids in the polymer layer and reducing its water permeability (WVTR of 5.1 x 10⁻³ g m⁻² day⁻¹ at 45°C-65% RH) and hydrophilicity. Their bilayer TFE design outperformed Al₂O₃-only encapsulated devices after 300 hours of aging at 45°C-65% RH, with the PDMS/Al₂O₃ devices experiencing less than an 8% relative drop in PCE. An organic-inorganic multilayer TFE structure is an even more effective approach for perovskite solar cell stability. Lee et al. combined a low-temperature (60°C) thermal ALD Al₂O₃ process

and poly(1,3,5-trimethyl-1,3,5-trivinyl cyclotrisiloxane) (pV3D3) grown at 40°C using initiated CVD (iCVD) to demonstrate impressive device stability under harsh testing conditions.¹⁶⁶ The WVTR for a nanolaminate consisting of 4 repeating units of pV3D3/Al₂O₃ was $5.3 \times 10^{-4} \text{ g m}^{-2} \text{ day}^{-1}$ in a 38°C-90% RH environment. The low water permeability of this multilayer TFE resulted in a retention of 97% of initial PCE for high-efficiency (18.2%) FA_{0.87}MA_{0.13}Pb(I_{0.87}Br_{0.13})₃ devices after exposure to 50°C-50% RH for 300 hours (**Figure 10c**). The improved stability associated with the nanolaminate TFE was likely due to a longer and more tortuous path for the diffusion of water molecules into the devices or for the effusion of volatile perovskite degradation products.

The use of molecular layer deposition (MLD) to grow hybrid organic-inorganic encapsulant materials is another promising approach to extend the lifetime of PSCs. Wang et al. used alternating cycles of TMA and ethylene glycol to grow alucone at 50°C directly on perovskite devices.¹⁶⁷ By itself, the hybrid alucone layer acted as a decent water barrier with a WVTR of $6.6 \times 10^{-3} \text{ g m}^{-2} \text{ day}^{-1}$ in a 30°C-80% RH environment. Its performance as an encapsulant was improved with the addition of PEALD Al₂O₃ in a bilayer structure. Typically, the O₂ plasma from PEALD would be incompatible with the underlying perovskite material (see Section 7). Yet, *in-situ* quadrupole mass spectroscopy (QMS) revealed that excess carbon in the alucone film protected the perovskite during PEALD by consuming O₂ plasma and forming CO₂ as a byproduct. The resulting WVTR of a double bilayer of alucone and PEALD Al₂O₃ was an impressive $1.6 \times 10^{-5} \text{ g m}^{-2} \text{ day}^{-1}$ at 30°C-80% RH. This encapsulation design allowed PSCs to maintain 95% of their initial efficiency after 300 min submerged in water and 96% of their initial efficiency after >2100 hours at 30°C and 80% RH.

There is still ample room for improvement of ALD- and CVD-based TFEs for perovskite solar cell applications. The exploration of new hybrid organic-inorganic materials (e.g. metalcones) and the development of single-reactor systems that can easily accommodate switching between the deposition of both organic and inorganic films are two avenue that could lead to a scalable encapsulation solution. In addition, a better understanding of how TFEs respond to applied mechanical stresses, as well as a set of standardized tests for comparing different TFE designs, are necessary to aid in this development. Nevertheless, a TFE solution via ALD/CVD could be the key to unlocking an array of new, dynamic applications for flexible perovskite solar cells.

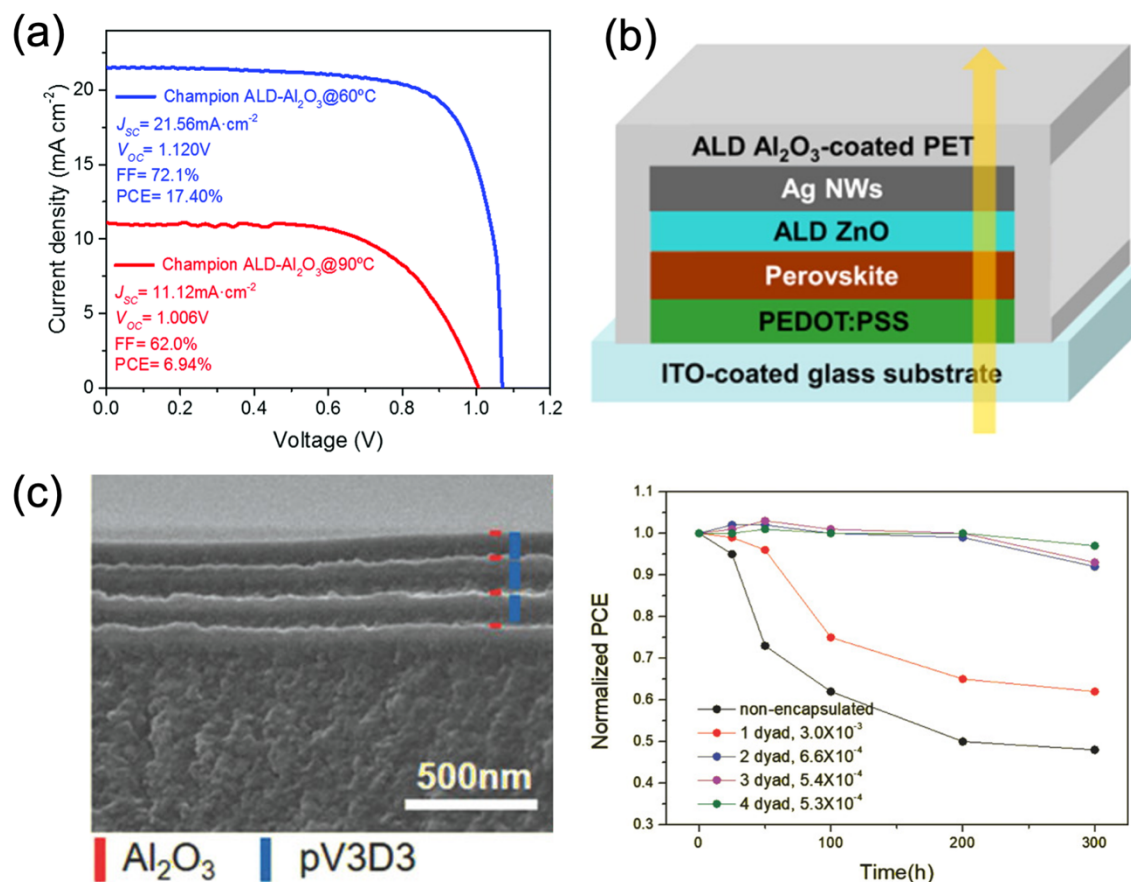


Figure 10: (a) J-V characteristics and the resulting performance parameter of mesoporous perovskite solar cells encapsulated with ~ 16 nm of ALD Al_2O_3 grown at 60°C (blue) and 90°C (red). Reproduced with permission.¹⁶³ Copyright 2018, The Royal Society of Chemistry. (b) Schematic of a semitransparent device encapsulated with ALD Al_2O_3 -coated PET, which retained, on average, >90% of its initial efficiency following 40 days of storage in ambient air (30°C-65% RH). Reproduced with permission.¹⁶⁴ Copyright 2015, American Chemical Society. (c) Cross-sectional SEM image of a TFE design consisting of alternating layers of iCVD pV3D3 and ALD Al_2O_3 . PCE stability over 300 hours at 50°C-50% RH for devices with 1-4 repeating dyads or bilayers of pV3D3/ Al_2O_3 . Reproduced with permission.¹⁶⁶ Copyright 2017, Wiley-VCH.

8. Compatibility of CVD/ALD on top of perovskite

For many of the applications discussed in the previous sections (e.g. passivation, contact, and buffer layers), CVD or ALD processing occurs after deposition of the perovskite material during device fabrication. In these cases, the perovskite is subjected to the environment inside the reactor during film growth. Elements such as temperature and co-reactant or precursor exposure all have the potential to alter the structure and composition, and consequently the optoelectronic properties, of the perovskite material. These effects are amplified in circumstances where CVD/ALD is grown directly on the perovskite without any interlayers.

The extent to which these interactions occur is also largely dependent up the CVD/ALD reaction chemistry and the initial composition of the perovskite film. An increase in the number of reports of ALD, in particular, on top of the perovskite in the past few years has prompted more fundamental and mechanistic studies of the interactions between metal halides perovskites and ALD precursors and co-reactants. In this section we will provide commentary only on these ALD reports, noting that similar effects are likely to occur for analogous CVD processes.

The most well studied system to date is ALD Al_2O_3 grown directly on the commonly used MAPbI_3 absorber. In practice, ultra-thin ALD Al_2O_3 layers are used in this capacity as passivation/barrier layers to improve the environmental stability of the perovskite in the presence of heat and moisture (Section 3.1).^{86,89,168–170} They have also replaced traditional contact layers on top of the perovskite to create metal-insulator-semiconductor (M-I-S) rear contacts.^{171,172} In all of these examples, the ALD Al_2O_3 is deposited at a low temperature ($<100^\circ\text{C}$) to minimize thermally induced stress on the perovskite material. Various co-reactants have been explored with inconsistent results. Kim et al. showed that a TMA and ozone-based ALD process resulted in a complete loss of the crystalline $\text{MAPbI}_{3-x}\text{Cl}_x$ phase and bleaching of the perovskite film.⁸⁷ They observed a similar, albeit less pronounced effect with H_2O as the co-reactant. These results compelled them to use a non-hydrolytic aluminum triisopropoxide (AIP) and acetic acid (AA) ALD process to stabilize the perovskite with an Al_2O_3 overlayer. X-ray diffraction (XRD) of $\text{MAPbI}_{3-x}\text{Cl}_x$ films exposed to 200 cycles of AIP and AA at 100°C confirmed no bulk formation of a crystalline PbI_2 degradation product. Zardetto et al. showed that O_2 plasma, even at a low deposition temperature of 30°C , is also too harsh of a co-reactant, causing partial bulk degradation of MAPbI_3 to PbI_2 .²⁸ However, unlike Kim et al., they did not observe any change to the crystallinity or surface composition of the perovskite upon exposure to repeated TMA/ H_2O cycles at 80°C . In particular, the XPS peaks corresponding to iodine and nitrogen from the methylammonium cation were unchanged following Al_2O_3 deposition.

Several other reports that probed the perovskite surface during and/or after ALD Al_2O_3 deposition by TMA and H_2O contradict the findings of Zardetto et al. One study in particular by Koushik et al. used the same XPS characterization to show that nitrogen is abstracted from the surface of the perovskite film during ALD Al_2O_3 deposition at 80°C .¹⁷³ This loss of nitrogen implies an etching of the methylammonium cation from the perovskite lattice. The authors also used *in-situ* infrared (IR) spectroscopy during ALD film growth (**Figure 11a**) and observed a reduction in the bands associated with the stretching and bending modes of N-H with an increasing number of ALD cycles, corroborating the XPS results. Koushik et al. went on to propose a mechanism for the initial reaction between TMA and the MAPbI_3 surface shown in **Figure 11b**. They hypothesized that in the first half cycle, the TMA molecule interacts with the methylammonium

cation, releasing methylamine and methane and forming a $\text{PbI}_3\text{-Al}(\text{CH}_3)_2$ adduct that further reacts with H_2O in the second half cycle to form -OH groups that can propagate Al_2O_3 growth in subsequent cycles. This mechanism was supported by in-depth density function theory calculations in an independent study by Choudhury et al.¹⁷⁴ Loss of N from the perovskite was observed for up to 200 ALD Al_2O_3 cycles, indicating that despite the formation of an Al_2O_3 overlayer, perovskite degradation products continue to effuse from the surface upon successive TMA pulses (**Figure 11c**). It is also important to note that despite the compositional changes observed at the perovskite surface, no bulk decomposition or structural changes to the perovskite were observed by XRD.

A recent paper by Yu et al. further investigated the etching of MAPbI_3 during thermal ALD of Al_2O_3 by exploring the effect of deposition temperature and TMA partial pressure.¹⁷⁵ They found via *in-situ* quartz crystal microbalance (QCM) measurements and QMS that TMA partial pressures as low as 0.1 torr will etch a MAPbI_3 film at 75°C , resulting in a nucleation delay of roughly ten cycles before Al_2O_3 begins to accumulate on the perovskite surface. By reducing the temperature to 25°C and maintaining the 0.1 torr TMA pulses, they observed steady Al_2O_3 growth from the onset. However, increasing the partial pressure of the TMA to 3 torr resulted in etching of the MAPbI_3 beyond just the surface region at 25°C , as was evident by a continual mass loss of perovskite with high TMA exposure. This study highlights that varying ALD process parameters can result in drastically different perovskite/metal oxide interfaces and suggests that discrepancies within the literature could be due to differences in deposition conditions across laboratories.

The compatibility of ALD SnO_2 growth on perovskites has also been evaluated recently, due to its extensive use for electron contacts and buffer layers in multijunction solar cells. In one study, Hultqvist et al. used TDMASn and H_2O to conformally deposit ALD SnO_2 directly onto a mixed cation, mixed halide $\text{MA}_x\text{FA}_{1-x}\text{PbBr}_y\text{I}_{1-y}$ perovskite.¹⁷⁶ Their XPS results indicated that a single 30 seconds of exposure to the TDMASn precursor at 120°C (>11 torr-s of total precursor exposure) does not alter the surface composition or bulk crystallinity of the perovskite. Yet, the performances of inverted solar cells that incorporated ALD SnO_2 as an electron contact were significantly lower than those of control devices with a PCBM electron contact. The highest reported efficiency was $\sim 4.0\%$ with 50 cycles of ALD SnO_2 , and the cells also displayed a significant amount of hysteresis. XPS depth profiling revealed that the perovskite/ SnO_2 interface was halide-rich, suggesting that the poor performance could be due to an energy barrier at the interface caused by undesirable perovskite/precursor interactions upon repeated ALD cycling. Palmstrom et al. also conducted a thorough investigation of the effects of ALD SnO_2 growth on perovskites and found further evidence of surface damage upon deposition.⁶³ Following 60 cycles of thermal ALD SnO_2 , they observed

a loss of nitrogen from the surface of a $\text{FA}_{0.17}\text{Cs}_{0.83}\text{PbBr}_{0.17}\text{I}_{0.83}$ film by XPS (**Figure 11d**), as well as the formation of PbI_2 and contraction of the perovskite lattice parameter by XRD. Their results also indicated that the TDMASn precursor has a stronger effect on perovskite degradation than either H_2O or temperature exposure up to 150°C . In contrast to the findings of Hultqvist et al.,¹⁷⁶ they observed the same PbI_2 formation and lattice contraction of the perovskite after 60 consecutive pulses of TDMASn (6 torr-s of total precursor exposure). These results imply removal of the formamidinium cation by TDMASn, similar to the etching effects reported for ALD Al_2O_3 . To avoid this issue, an organic ETL (e.g. C_{60}) is typically used as an interfacial layer to protect the perovskite from ALD SnO_2 precursor damage. Other strategies, such as using a pulsed-CVD process with shorter purge times, can also reduce exposure of the perovskite to the ALD precursor during contact layer deposition.⁶³

Several other ALD metal oxides with applications as electron or hole contacts were tested by Zardetto et al. on perovskite substrates, including O_2 plasma-based TiO_2 , MoO_x , and NiO , as well as thermal ZnO .²⁸ All three of the O_2 plasma-based processes altered the surface chemistry of a MAPbI_3 film, including a complete loss of nitrogen and iodine oxidation as determined by XPS. This extent of surface modification does not bode well for the successful application of these processes in working perovskite solar cells. Interestingly, the thermal ALD ZnO process, consisting of cycles of DEZ and H_2O , also presented its own issues. In addition to causing significant degradation of the MAPbI_3 substrate, the ZnO did not appear to grow on the perovskite substrate;²⁸ this finding was also observed by Hultqvist et al.¹⁷⁶ Further research is required to understand what inhibits nucleation of ALD ZnO on the perovskite surface.

The complexity associated with different ALD metal oxide processes and the large number of accessible perovskite compositions make it challenging to predict how the two components will interact and if the resulting interface will translate to an efficient and stable solar cell. This difficulty is evident by the often-conflicting results published in the literature. However, some general guidelines can be formed based on the existing reports. For the systems already studied, it appears that low temperature ($<100^\circ\text{C}$), thermal processes (i.e. with H_2O as the co-reactant) are preferred to achieve more stable interfaces and avoid bulk perovskite degradation. Additionally, it appears that metal-organic ALD precursors can react with organic cations in the perovskite film altering its surface composition and structure even at lower temperatures. The development of more sensitive, *in-situ* characterization techniques, such as ultraviolet photoelectron spectroscopy and photoluminescence, are needed to uncover how these changes affect optoelectronic properties at the perovskite/ALD interface. While organic interlayers can limit damage associated with ALD processing, there is a strong desire to find alternatives because of the high costs and low stability

associated with them. Strategies aimed at stabilizing the perovskite surface prior to ALD could help achieve this goal and enable the deposition of inorganic contacts directly on top of the perovskite active layer.

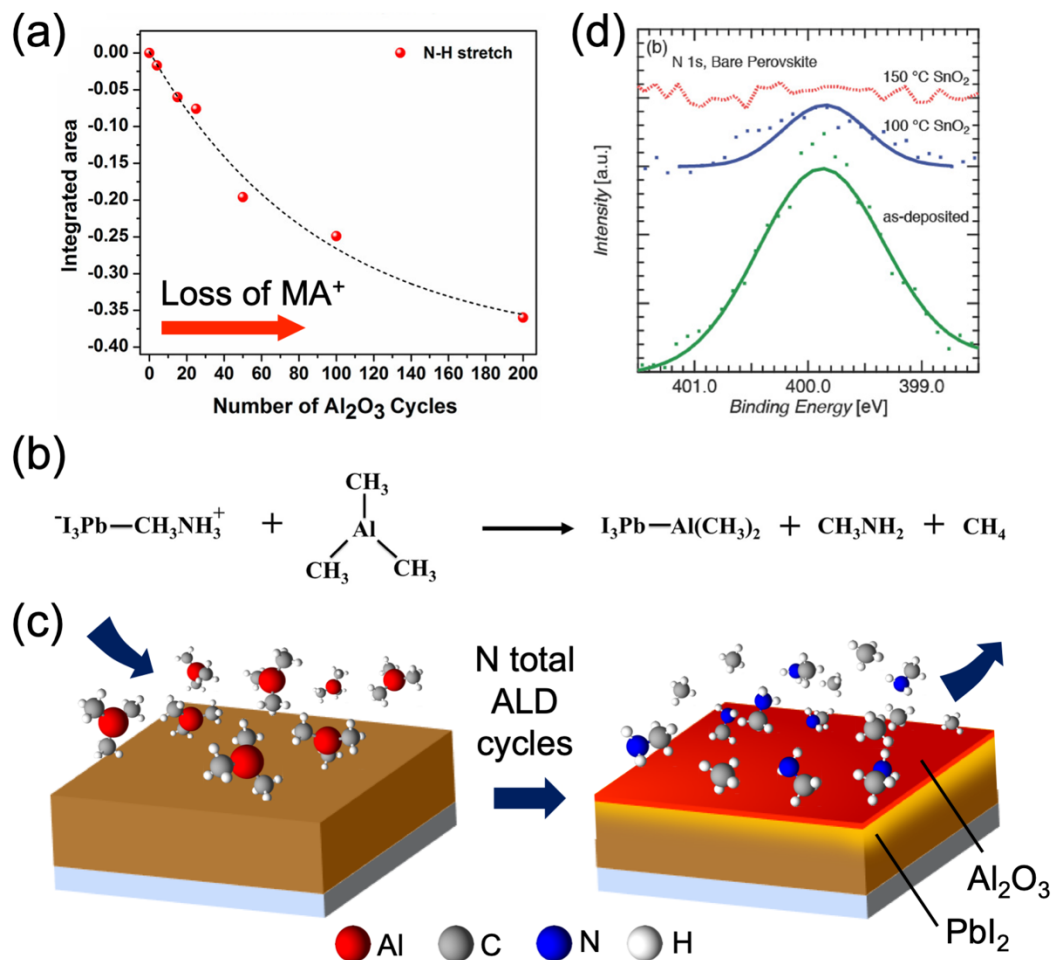


Figure 11: (a) Integrated area of the N-H stretching mode from *in-situ* differential infrared (IR) spectra of a $\text{MAPI}_{3-x}\text{Cl}_x$ perovskite film following various ALD cycles numbers with TMA and H_2O to form an Al_2O_3 overlayer. (b) Proposed reaction mechanism between TMA and MAPbI_3 in the first half-cycle of an ALD Al_2O_3 process.¹⁷³ Reproduced and adapted with permission. Copyright 2019, American Chemical Society. (c) Pictorial representation of the effect of numerous cycles of ALD Al_2O_3 growth with TMA directly on a metal halide perovskite absorber. (d) High-resolution XPS spectra of the N1s peak for an as-deposited $\text{FA}_{0.17}\text{Cs}_{0.83}\text{PbBr}_{0.17}\text{I}_{0.83}$ film, as well as for films following 60 cycles of ALD SnO_2 ($\text{TDMASn} + \text{H}_2\text{O}$) at both 100°C and 150°C. Reproduced with permission.⁶³ Copyright 2018, Wiley-VCH.

9. Conclusions & Outlook

The versatility of CVD and ALD makes them useful tools for the fabrication of many components of PSCs. In this review, we highlighted the effectiveness of these vapor deposition techniques for improving both device efficiency and stability. In addition to their use for the synthesis of perovskite absorbers, contact

layers, and electrodes, CVD and ALD can provide effective passivation of interfaces to reduce defects and improve charge collection. ALD buffer layers and interconnects have enabled the fabrication of impressive, high-efficiency multi-junction solar cells while also contributing to improved stability. Additionally, device lifetimes can be further extended by employing low-temperature, hybrid CVD/ALD encapsulation schemes.

Based on the literature to date, there are several trends in the application of CVD and ALD to PSCs that can inform future research and development in the field. First, significant effort thus far has focused on improving the performance of ALD-grown ETLs, particularly TiO_2 and SnO_2 . Some strategies that have been implemented include tuning ALD parameters to achieve a desired phase or film thickness and *in-situ* doping of the ETL to improve its conductivity. Less attention has been given to developing new or improving existing CVD/ALD HTL materials. This discrepancy is likely due to the fact that most early research focused on PSCs in the n-i-p architecture. In this structure, the ETL is deposited first as a substrate and as a result, CVD/ALD processing conditions are not limited by the instability of the perovskite absorber (see Section 8). Recently, however, researchers have shown that similar high efficiencies can be achieved with p-i-n PSCs. For this reason, we expect significantly more exploration of CVD/ALD HTLs in the coming years. This research could include the development of novel precursor chemistries or the investigation of ternary or quaternary materials.

Next, we recognize the important role that contact layers play in stabilizing PSCs for long-term operation. For a perovskite module to last for an extended period of time in the field, it must be resilient to both internal and external stressors. While an effective encapsulation scheme can eliminate exposure to air, moisture and UV light, it does not prevent against reactions that can occur between various layers of the device. Organic contact layers, including polymers and small molecules, are widely used in PSCs; however, they are typically insufficient for arresting the diffusion of reactive species (e.g., metal from the electrodes) throughout the device and can be intrinsically unstable, for example when exposed to heat. Inorganic ALD and CVD contact layers can be used in conjunction with or completely replace organic contacts to act as ‘built-in’ barrier layers. ALD contacts, in particular, are uniquely suited and the ideal choice for this application because of their conformality and density at low film thicknesses. In PSC modules, they can also help protect areas of the perovskite absorber that become exposed when using scribe lines to create interconnects between subcells.²⁵

Continued development of high-throughput reactors will ensure that advances made in the laboratory translate to PSCs at the industrial scale. While some high-throughput CVD/ALD reactors are currently

available commercially, the set of materials they can grow is still quite limited. Breakthroughs in design to accommodate plasma-enhanced growth or organic precursors are needed to enhance the capability of these tools. Integrating *in-situ* characterization techniques into reactors can also greatly expedite new process development. As interest in CVD and ALD for PSC applications has grown, there has been an increase in the number of studies aimed at understanding how CVD/ALD conditions affect the interfacial and bulk chemical properties of metal halide perovskite materials (see Section 8). Again, these preliminary studies have been limited to only a few precursor chemistries and perovskite compositions. Broader studies that incorporate more CVD/ALD processes and also characterize changes to the electronic structure of the perovskite are needed.

Lastly, CVD and ALD have expanded the utility of PSCs considerably in the past few years. Tandem solar cells that incorporate perovskite sub-cells continue to climb in efficiency and are a promising entry to market for the technology in a competitive solar PV industry. ALD/CVD buffer layers and interconnects have been instrumental in the success of these tandem devices thus far (see Section 6), again relying upon the conformality and density of the resultant films. Going forward, we foresee that ALD and CVD will also contribute to the application of PSCs in emerging solar markets (**Figure 12**). For example, the growing transportation industry, internet-of-things, wearable electronics, and portable water purification systems could all benefit from lightweight, flexible modules that have the same reliability as traditional, rigid modules with glass encapsulation. Hybrid TFEs that combine both ALD and CVD layers are gaining traction in the organic electronics industry and should be considered for these flexible PSCs as well.

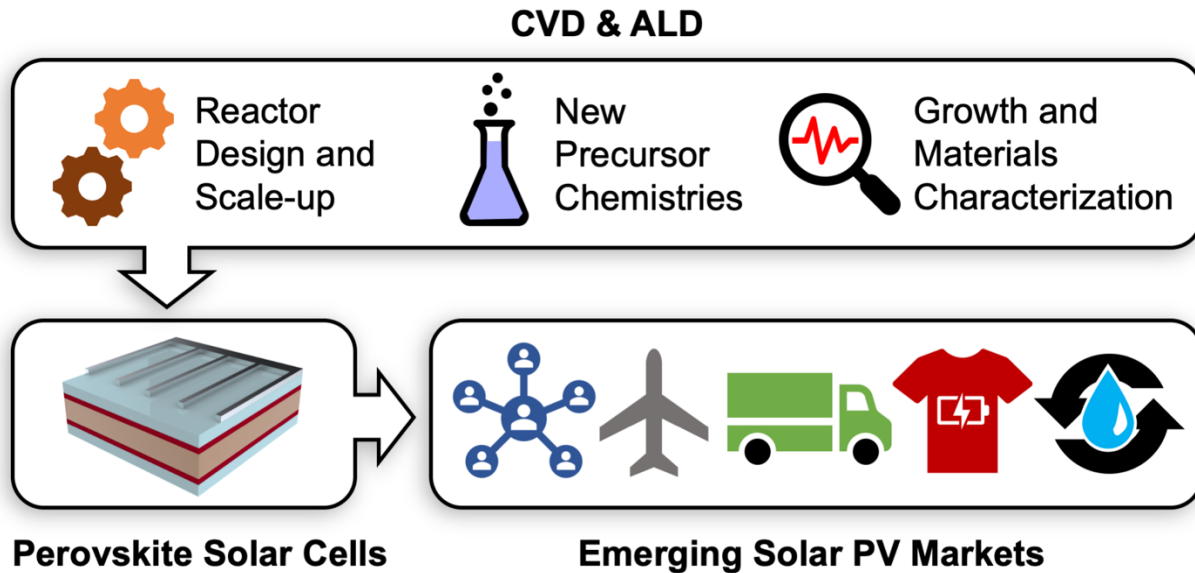


Figure 12: Future research directions for CVD and ALD applied to perovskite solar cells include advances in reactor design and throughput, new and improved materials based on precursor development, and further understanding of material/interface properties through advanced characterization techniques. Breakthroughs in these areas can help propel PSCs into emerging solar PV markets including the internet-of-things, transportation, wearable electronics, and portable water purification systems.

Acknowledgments

This work was supported by the U.S. Department of Energy (DOE) Office of Energy Efficiency and Renewable Energy (EERE) under Solar Energy Technologies Office (SETO) Agreement Number DE-EE0008167 (JAR). This work was also supported by the U.S. DOE under award number DE-SC0004782 (SFB). S.T.O. acknowledges support from the Knight-Hennessy scholarship program for graduate study at Stanford University.

Table 1: List of ALD processes applied to Perovskite Solar Cells

Material	Precursors	Temperature (°C)	Application(s)	Absorber	Device Structure	J _{sc} (mA/cm ²)	V _{oc} (mV)	FF (%)	PCE (%)	Reference
Al ₂ O ₃	AIP + acetic acid	100	passivation	MAPbI _{3-x} Cl _x	--	--	--	--	--	87
Al ₂ O ₃	DMAI + H ₂ O	100	passivation	Cs _{0.15} FA _{0.85} Pb(I _{0.71} Br _{0.29}) ₃	n-i-p (P)	15.4	1220	73.4	13.8	90
Al ₂ O ₃	TMA + H ₂ O	25	passivation	MAPbI ₃	n-i-p (P)	16.5	1050	71	12.4	169
Al ₂ O ₃	TMA + H ₂ O	25	passivation	MAPbI ₃	n-i-p (P)	--	--	--	9.4	177
Al ₂ O ₃	TMA + H ₂ O	100	passivation	MAPbI _{3-x} Cl _x	n-i-p (P)	19.0	910	65	11.2	86
Al ₂ O ₃	TMA + H ₂ O	100	passivation	MAPbI _{3-x} Cl _x	n-i-p (P)	21.7	1070	77	18.0	89
Al ₂ O ₃	TMA + H ₂ O	100	passivation	MAPbI ₃	n-i-p (M)	17.6	921	68.4	11.1	171
Al ₂ O ₃	TMA + H ₂ O	120	passivation	MA _x FA _{1-x} Pb(I _y Br _{1-y}) ₃	n-i-p (M)	21.7	1080	72	16.9	83
Al ₂ O ₃	TMA + H ₂ O	150	passivation	MAPbI ₃	n-i-p (M)	18.9	1010	62	15.6	88
Al ₂ O ₃	TMA + H ₂ O	200	passivation	FA _{0.85} MA _{0.15} Pb(I _{0.85} Br _{0.15}) ₃	n-i-p (M)	22.8	1060	67	16.2	178
Al ₂ O ₃	--	--	passivation	MAPbI ₃	n-i-p (N)	22.4	1023	71.4	16.8	85
AZO	TMA/DEZ + H ₂ O	85	interconnecting layer ^{†*}	FA _{0.6} Cs _{0.3} DMA _{0.1} PbI _{2.4} Br _{0.6}	p-i-n (P)	15.6 [‡]	1820 [‡]	75 [‡]	21.3 [‡]	128
AZO	TMA/DEZ + H ₂ O	100	EC	Cs _{0.05} MA _{0.95} PbI ₃	p-i-n (P)	20.7	1025	79.2	16.8	179
GaN	TEG + Ar/N ₂ /H ₂ plasma	280	EC	FA _{0.85} MA _{0.15} Pb(I _{0.85} Br _{0.15}) ₃	n-i-p (P)	22.6	977	68.9	15.2	180
Ga ₂ O ₃	Ga ₂ (NMe ₂) ₆ + H ₂ O	120	passivation	MAPbI ₃	p-i-n (P)	22.41	1115	79.4	19.9	181
HfO ₂	TEMAHF + H ₂ O	90	passivation*	Cs _{0.05} (FA _{0.83} MA _{0.17}) _{0.95} Pb(I _{0.83} Br _{0.17}) ₃ (1 mol% RbI, 4 mol% KI additives)	n-i-p (P)	21.2	1135	79.2	19.1	82
NiO	Ni(dmamb) ₂ + O ₃	120-240	HC	MAPbI ₃	p-i-n (P)	21.9	1040	72	16.4	77
NiO	Ni(dmamb) ₂ + O ₃	200	HC	Cs _{0.05} MA _{0.95} PbI ₃	p-i-n (P)	20.7	1025	79.2	16.8	179
NiO	Ni(MeCp) ₂ + O ₂	350	HC ^S	FA _{0.2} MA _{0.8} PbI ₃	p-i-n (P)	23.0	1.08	81	17.1	74
NiO	Ni(MeCp) ₂ + O ₂ plasma	150	HC	Cs _{0.05} (MA _{0.17} FA _{0.83})PbI _{1.1} (I _{0.83} Br _{0.17}) ₃	p-i-n (P)	21.8	1070	73.4	17.1	75
NiO	Ni(MeCp) ₂ + O ₂ plasma	150	HC [#]	Cs _{0.05} (FA _{0.83} MA _{0.17}) _{0.95} Pb(I _{0.83} Br _{0.17}) ₃	p-i-n (P)	20.4	1090	75.2	16.7	148
PbI ₂	Pb(btsa) ₂ + SnI ₄	70-90	perovskite precursor	MAPbI ₃	--	--	--	--	--	182
PbS	Pb(tmhd) ₂ + H ₂ S	150	perovskite precursor	MAPbI ₃	--	--	--	--	--	122
SnO ₂	TDMASn + H ₂ O	80-150	EC, buffer layer	FA _{0.83} Cs _{0.17} Pb(I _{0.83} Br _{0.17}) ₃	p-i-n (P)	19.9	940	59.4	11.1	63
SnO ₂	TDMASn + H ₂ O	80	EC ^S	MAPbI ₃	p-i-n (P)	18.6	880	77.7	12.7	70
SnO ₂	TDMASn + H ₂ O	80	EC, buffer layer [#]	Cs _{0.05} (FA _{0.83} MA _{0.17}) _{0.95} Pb(I _{0.83} Br _{0.17}) ₃	p-i-n (P)	18.0 [#]	1590 [#]	75.7 [#]	21.6 [#]	148
SnO ₂	TDMASn + H ₂ O	80	EC	MAPbI ₃	p-i-n (P)	18.1	950	74.3	12.8	183
SnO ₂	TDMASn + H ₂ O	80	transparent electrode	MAPbI ₃	p-i-n (P)	17.9	860	73	11.2	184
SnO ₂	TDMASn + H ₂ O	100	EC, buffer layer [†]	Cs _{0.15} (FA _{0.83} MA _{0.17}) _{0.85} Pb(I _{0.8} Br _{0.2}) ₃	p-i-n (P)	17.8 [†]	1800 [†]	79.4 [†]	25.4 [†]	142
SnO ₂	TDMASn + H ₂ O	100	buffer layer [†]	C _s FA _{1-x} Pb(Br _y I _{1-y}) ₃	p-i-n (T)	18.4	1046	59.6	11.5	144
SnO ₂	TDMASn + H ₂ O	100	buffer layer [†]	C _s FA _{1-x} Pb(Br _y I _{1-y}) ₃	p-i-n (T)	19.5 [†]	1741 [†]	74.7 [†]	25.4 [†]	155
SnO ₂	TDMASn + H ₂ O	118	EC, interconnecting layer [†]	MA _x FA _{1-x} Pb(I _y Br _{1-y}) ₃	n-i-p (P)	20.1	1130	68.3	15.5	158
SnO ₂	TDMASn + H ₂ O	185	EC	MAPbI ₃	n-i-p (P)	23.0	1070	75	18.3	185
SnO ₂	TDMASn + O ₂ plasma	50-200	EC	Cs _{0.05} (FA _{0.83} MA _{0.17}) _{0.95} Pb(I _{0.9} Br _{0.1}) ₃	n-i-p (P)	22.1	1078	75.0	17.8	186
SnO ₂	TDMASn + O ₂ plasma	100	EC [‡]	FA _{0.3} MA _{0.7} PbI ₃	n-i-p (P)	20.1	1141	80	18.3	151
SnO ₂	TDMASn + O ₂ plasma	100	EC*	MA _{0.7} FA _{0.3} PbI ₃	n-i-p (P)	22.1	1101	75.4	18.4	187,188

SnO ₂	TDMASn + O ₂ plasma	100	EC	MA _{0.7} FA _{0.3} PbI ₃	n-i-p (P)	22.6	1128	80.0	20.4	189
SnO ₂	TDMASn + O ₃	100	EC	MAPbI ₃	n-i-p (P)	22.6	1070	75.6	18.3	69
SnO ₂	TDMASn + O ₃	100-120	EC, passivation	FA _{0.85} MA _{0.15} Pb(I _{0.85} Br _{0.15}) ₃	n-i-p (P)	22.7	1130	78	20.0	190
SnO ₂	TDMASn + O ₃	118	EC	FA _{0.85} MA _{0.15} Pb(I _{0.85} Br _{0.15}) ₃	n-i-p (P)	21.3	1140	74	18.4	68
SnO ₂	TDMASn + O ₃	118	EC	CS _{0.05} (FA _{0.83} MA _{0.17}) _{0.95} Pb(I _{0.83} Br _{0.17}) ₃	n-i-p (P)	23	1170	71	~20	191
SnO ₂	TDMASn + O ₃	118	EC	CS _{0.05} (FA _{0.83} MA _{0.17}) _{0.95} Pb(I _{0.83} Br _{0.17}) ₃	n-i-p (P)	--	--	--	~18	192
SnO ₂	TDMASn + H ₂ O TDMASn + O ₃ TDMASn + O ₂ plasma	100	EC	MAPbI ₃	n-i-p (P)	19.8 20.1 20.0	1040 1170 1120	51 59 60	10.6 13.9 13.3	193
SnO ₂	TDMASn + H ₂ O	--	EC, buffer layer [†]	CS _{0.05} (FA _{0.83} MA _{0.17}) _{0.95} Pb _{1.1} (I _{0.83} Br _{0.17}) ₃	p-i-n (P)	18.5 [†]	1760 [†]	78.5 [†]	25.5 [†]	143
SnO ₂ /ZTO	TDMASn/DEZ + H ₂ O	85	EC, buffer layer [‡]	CS _{0.05} FA _{0.8} MA _{0.15} PbI _{2.55} Br _{0.45}	p-i-n (P)	20.8	1124	79.3	18.5	150
SnO ₂ /ZTO	TDMASn/DEZ + H ₂ O	85	EC, buffer layer [#]	(FA _{0.65} MA _{0.20} CS _{0.15})Pb(I _{0.8} Br _{0.2}) ₃ (1 mol% PEAI, 2 mol% Pb(SCN) ₂ additives)	p-i-n (P)	19.6	1137	76.8	17.1	154
SnO ₂ /ZTO	TDMASn/DEZ + H ₂ O	90	EC	FA _{0.75} CS _{0.25} Pb(I _{0.80} Br _{0.12}) ₃	p-i-n (P)	19.7	1154	81.8	18.6	194
SnO ₂ /ZTO	TDMASn/DEZ + H ₂ O	100	EC, buffer layer [†]	FA _{0.83} CS _{0.17} Pb(I _{0.83} Br _{0.17}) ₃	p-i-n (P)	18.7	980	78.8	14.5	140
SnO ₂ /ZTO	TDMASn/DEZ + H ₂ O	100	EC, buffer layer [†]	FA _{0.75} CS _{0.25} Pb(I _{0.8} Br _{0.2}) ₃	p-i-n (P)	19.6	1050	77	15.8	141
SnO ₂ /ZTO	TDMASn/DEZ + H ₂ O	100	EC, interconnecting layer, buffer layer [‡]	FA _{0.83} CS _{0.17} Pb(I _{0.83} Br _{0.17}) ₃	p-i-n (P)	20.3	970	79	15.7	149
SnO ₂ /ZTO	TDMASn/ZTO + H ₂ O	100	EC, buffer layer	MAPbI ₃	p-i-n (P)	19.5	1020	67	12.8	195
SnO ₂ /ZTO	TDMASn/ZTO + H ₂ O	100	EC, buffer layer [‡]	FA _{0.6} CS _{0.4} Pb(I _{0.7} Br _{0.3}) ₃	p-i-n (P)	14.8 [‡]	1810 [‡]	70 [‡]	19.1 [‡]	196
TiN	TiCl ₄ + NH ₃	350	passivation	MA _{0.17} FA _{0.83} Pb(I _{0.83} Br _{0.17}) ₃	n-i-p (M)	22.5	1135	75.0	19.0	91
TiO ₂	TiCl ₄ + H ₂ O	100-300	EC	MAPbI ₃	n-i-p (M)	--	--	--	11.4	197
TiO ₂	TiCl ₄ + H ₂ O	150	EC	MAPbI ₃	n-i-p (P)	20.2	1040	73	15.1	198
TiO ₂	TiCl ₄ + H ₂ O	150-250	EC	MAPbI _{3-x} Cl _x	n-i-p (P)	18.1	940	68	11.6	199
TiO ₂	TiCl ₄ + H ₂ O	300	EC	MAPbI ₃	n-i-p (M)	20.8	1030	70.2	15.0	200
TiO ₂	TiCl ₄ (no co-reactant reported)	--	EC	MAPbI ₃	n-i-p (P,M)	16.6	1010	72.3	12.1	201
TiO ₂	Ti(CpMe)(NMe ₂) ₃ + H ₂ O	150	passivation*	MA _{0.1} FA _{0.75} CS _{0.15} PbI _{2.9} Br _{0.1}	n-i-p (P)	22.45	1030	74	17.1	202
TiO ₂	Ti(CpMe)(NMe ₂) ₃ + O ₂ plasma	150	EC*	MAPbI _{3-x} Cl _x	n-i-p (M)	14.1	858	70	8.4	203
TiO ₂	Ti(CpMe)(NMe ₂) ₃ + O ₂ plasma	150	EC	MAPbI ₃	n-i-p (M)	19.6	1048	77	15.9	204
TiO ₂	Ti(CpMe)(NMe ₂) ₃ + O ₂ plasma	150	EC*	MAPbI _{3-x} Cl _x	n-i-p (M)	14.9	882	70	9.2	205
TiO ₂	TDMAT + H ₂ O	60	EC	MAPbI ₃	p-i-n (P)	22.8	1040	76.9	18.3	66
TiO ₂	TDMAT + H ₂ O	70	EC	CS _{0.05} (FA _{0.83} MA _{0.17}) _{0.95} Pb(I _{0.83} Br _{0.17}) ₃	p-i-n (P)	--	--	--	13.2	206
TiO ₂	TDMAT + H ₂ O	80	EC	MAPbI _{3-x} Cl _x	n-i-p (M,P)	21.5	920	60.3	12.5	207
TiO ₂	TDMAT + H ₂ O	80	EC	MAPbI _{3-x} Cl _x	n-i-p (P)	24.3	980	57.1	13.6	208
TiO ₂	TDMAT + H ₂ O	100	EC	CS _{0.05} MA _{0.95} PbI ₃	p-i-n (P)	19.6	1020	70.2	14.0	179
TiO ₂	TDMAT + H ₂ O	120	EC	MAPbI ₃	n-i-p (P)	23.5	1060	73.4	18.2	61
TiO ₂	TDMAT + H ₂ O	120	EC	MAPbI ₃	n-i-p (M)	23.1	1081	73.4	18.3	62
TiO ₂	TDMAT + H ₂ O	120	EC	MAPbI _{3-x} Cl _x	p-i-n (P)	19.7	930	47.7	8.8	209
TiO ₂	TDMAT + H ₂ O	120	EC	CsPbI ₂ Br	n-i-p (P)	10.9	1273	66	9.3	210
TiO ₂	TDMAT + H ₂ O	120	passivation	MAPbI ₃	n-i-p (M)	17.6	969	67	11.5	211
TiO ₂	TDMAT + H ₂ O	150	EC, interconnecting layer [†]	CS _{0.05} Rb _{0.05} FA _{0.765} MA _{0.135} PbI _{2.55} Br _{0.45}	n-i-p (M)	17.8 [†]	1762 [†]	78.1 [†]	24.5 [†]	146

TiO ₂	TDMAT + H ₂ O	150	EC [†]	MAPbI ₃	n-i-p (M)	11.5 [†]	1580 [†]	75 [†]	13.7 [†]	159
TiO ₂	TDMAT + H ₂ O	150	EC	FA _{0.3} MA _{0.7} PbI _{3-x} Cl _x	n-i-p (P)	23.0	1083	78.2	19.5	212
TiO ₂	TDMAT + H ₂ O	150	EC	MAPbI _{3-x} Cl _x	n-i-p (P)	20.5	1070	75.2	16.5	213
TiO ₂	TDMAT + H ₂ O	165	EC	MAPbI ₃	n-i-p (P)	21.7	960	42.2	8.8	69
TiO ₂	TDMAT + H ₂ O	185	EC	MAPbI ₃	n-i-p (M,P)	19.8	1097	70.6	15.3	185
TiO ₂	TDMAT + H ₂ O	200	EC	--	n-i-p (M)	18.7	930	72	12.6	60
TiO ₂	TDMAT + H ₂ O	225	EC	MAPbI ₃	n-i-p (M)	22.3	1110	74	18.4	214
TiO ₂	TDMAT + H ₂ O	--	EC	MAPbI ₃	n-i-p (N)	23.8	1100	77	20.1	215
TiO ₂	TTIP + acetic acid	100	passivation	MAPbI _{3-x} Cl _x	--	--	--	--	--	87
TiO ₂	TTIP + H ₂ O	150	EC	MAPbI ₃	n-i-p (M)	19.5	965	41.5	7.8	216
TiO ₂	TTIP + H ₂ O	250	passivation	MAPbI ₃	n-i-p (N)	19.8	945	72	13.5	93
TiO ₂	TTIP + H ₂ O	--	EC	MASnIBr ₂	n-i-p (M)	12.3	820	57	5.73	217
TiO ₂	TTIP + O ₂ plasma	80	EC*	MAPbI _{3-x} Cl _x	n-i-p (P)	21.4	950	60	12.2	218
TiO ₂	TTIP + O ₂ plasma	130	EC	MAPbI ₃	n-i-p (P)	20.3	1033	75.5	15.8	219
TiO ₂	--	120	passivation	MAPbI ₃	n-i-p (N)	22.1	975	65	13.4	220
TiO ₂ -IrO _x	TDMAT + H ₂ O (EtCp)Ir(CHD) + O ₃	175	HC	FA _{0.83} Cs _{0.17} Pb(I _{0.83} Br _{0.17}) ₃	p-i-n (P)	19.6	1005	80	15.8	80
VO _x	V(dma) ₄ + H ₂ O	50	HC	MAPbI ₃	p-i-n (P)	17.9	900	71.2	11.5	78
VO _x	VTIP + H ₂ O	80	HC, buffer layer	FA _{0.83} Cs _{0.17} Pb(I _{0.83} Br _{0.17}) ₃	n-i-p (P)	18.9	1070	71	14.2	79
ZnO	DEZ + H ₂ O	70	EC	MAPbI ₃	n-i-p (M)	20.4	976	66	13.1	221
ZnO	DEZ + H ₂ O	80	EC, buffer layer	MAPbI ₃	p-i-n (P)	20.7	1020	76.4	16.2	164
ZnO	DEZ + H ₂ O	95	buffer layer ^{S,†}	Cs _{0.05} (FA,MA) _{0.95} Pb(I _{0.9} Br _{0.1}) ₃	p-i-n (P)	19.8	996	73.1	14.5	222
ZnO	DEZ + H ₂ O	150	EC	MAPbI ₃	n-i-p (M)	18.9	1010	62	15.6	88
ZnO	DEZ + H ₂ O	150	EC	MAPbI ₃	n-i-p (M)	18.5	759	50	7.0	223
ZnS	DEZ + H ₂ S	150	passivation	FA _{0.85} MA _{0.15} Pb(I _{0.85} Br _{0.15}) ₃	n-i-p (M)	22.5	1130	75	18.8	224
ZrO ₂	TDMAZr + O ₃	80	passivation	MAPbBr ₃	p-i-n (P)	7.7	1653	79	10.1	92

EC = electron contact, HC = hole contact, * = flexible, ^S = spatial ALD
 Integrated into a tandem solar cell with silicon (†), perovskite (‡) or CIGS (#)
 P = planar, M = mesoscopic, N = nanostructured, T = textured

Device statistics are for single-junction cells scanned in the reverse direction from V_{OC} to J_{SC}, unless noted otherwise.

Table 2: ALD Encapsulation for Perovskite Solar Cells

Material	Precursors	Temperature (°C)	Absorber	Device Structure	Stability Test Conditions	Initial PCE (%) (% PCE remaining after stability test)	Reference
Al ₂ O ₃	TMA + H ₂ O	60	MAPbI ₃	p-i-n (P)	Ambient air, 40-60% RH, RT, dark, 1000 hr	-- (93%)	66
Al ₂ O ₃	TMA + H ₂ O	60-90	MAPbI ₃	n-i-p (M)	Ambient air, ~80% RH, RT, dark, 2256 hr	16.4 (76%)	163
Al ₂ O ₃	TMA + O ₃	70	MAPbI ₃	n-i-p (P)	Ambient air, RT, dark, 576 hr	14.3 (90%)	168
Al ₂ O ₃	TMA + H ₂ O	75	Cs _{0.05} (FA _{0.83} MA _{0.17}) _{0.95} PbI _{2.5} Br _{0.5}	n-i-p (P)	Ambient air, RT, dark, 7200 hr	19.4 (~87.5%)	225
Al ₂ O ₃	TMA + H ₂ O TMA + O ₂ plasma	95	FA _{0.85} MA _{0.15} Pb(I _{0.85} Br _{0.15}) ₃	n-i-p (M)	Atmosphere not reported, 50% RH, RT, dark, 7500 hr	-- (96%)	162
Al ₂ O ₃ (with MLD alucone)	TMA + O ₂ plasma TMA + Ethylene Glycol (EG)	50	MAPbI ₃	n-i-p (P)	80% RH, 30°C, 2100 hr	~17% (96%)	167
Al ₂ O ₃ (with CVD pV3D3)	TMA + H ₂ O	60-120	FA _{0.87} Cs _{0.13} Pb(I _{0.87} Br _{0.13}) ₃	n-i-p (M)	N ₂ atmosphere, 50% RH, 50°C, dark, 300 hr	18.6 (97%)	166
Al ₂ O ₃ (with PDMS)	TMA + H ₂ O	95	FA _{0.85} MA _{0.15} Pb(I _{0.85} Br _{0.15}) ₃	n-i-p (M)	Atmosphere not reported, 65% RH, 45°C, dark, 300 hr	-- (95%)	165
Al ₂ O ₃ (coated on PET)	TMA + H ₂ O	100	MAPbI ₃	p-i-n (P)	Ambient air, 65% RH, 30°C, dark, 1000 hr	10.6 (>90%)	164
Al ₂ O ₃ and AZO	TMA + H ₂ O TMA/DEZ + H ₂ O	100 100	Cs _{0.05} MA _{0.95} PbI ₃	p-i-n (P)	Ambient air, 20-60% RH, RT, 1 sun illumination with a 420 nm cutoff UV filter, 500 hr	15.6 (99.5%)	179
Al ₂ O ₃ and AZO	TMA + H ₂ O TMA/DEZ + H ₂ O	100 100	Cs _{0.05} MA _{0.95} PbI ₃	p-i-n (P)	Ambient air, 20-60% RH, 85°C, 1 sun illumination with a 420 nm cutoff UV filter, near-MPP, 500 hr	16.5 (86.7%)	179
Ga ₂ O ₃	Ga ₂ (NMe ₂) ₆ + H ₂ O	120	MAPbI ₃	p-i-n (P)	Ambient air, ~40% RH, RT, dark, 480 hr	18.5 (84%)	181
TiO ₂	TDMAT + H ₂ O	70	Cs _{0.05} (FA _{0.83} MA _{0.17}) _{0.95} Pb(I _{0.83} Br _{0.17}) ₃	p-i-n (P)	Ambient air, RT, dark, 150 hr	13.2 (45%)	206
TiO ₂	TDMAT + H ₂ O	120	MAPbI _{3-x} Cl _x	p-i-n (P)	Ambient air, 100°C, dark, 10 hr	8.8 (91%)	209

RT = room temperature

RH = relative humidity

MPP = maximum power point

MLD = molecular layer deposition

References

- 1 National Renewable Energy Laboratory, Best Research-Cell Efficiencies, <https://www.nrel.gov/pv/cell-efficiency.html>, (accessed 8 January 2020).
- 2 S.-H. Turren-Cruz, A. Hagfeldt and M. Saliba, *Science*, 2018, **362**, 449–453.
- 3 K. A. Bush, K. Frohna, R. Prasanna, R. E. Beal, T. Leijtens, S. A. Swifter and M. D. McGehee, *ACS Energy Lett.*, 2018, **3**, 428–435.
- 4 M. Saliba, T. Matsui, J.-Y. Seo, K. Domanski, J.-P. Correa-Baena, M. K. Nazeeruddin, S. M. Zakeeruddin, W. Tress, A. Abate, A. Hagfeldt and M. Grätzel, *Energy Environ. Sci.*, 2016, **9**, 1989–1997.
- 5 J. H. Noh, S. H. Im, J. H. Heo, T. N. Mandal and S. Il Seok, *Nano Lett.*, 2013, **13**, 1764–1769.
- 6 G. E. Eperon, S. D. Stranks, C. Menelaou, M. B. Johnston, L. M. Herz and H. J. Snaith, *Energy Environ. Sci.*, 2014, **7**, 982.
- 7 M. I. H. Ansari, A. Qurashi and M. K. Nazeeruddin, *J. Photochem. Photobiol. C Photochem. Rev.*, 2018, **35**, 1–24.
- 8 S. Sun, T. Buonassisi and J. Correa-Baena, *Adv. Mater. Interfaces*, 2018, **5**, 1800408.
- 9 Z. H. Bakr, Q. Wali, A. Fakharuddin, L. Schmidt-Mende, T. M. Brown and R. Jose, *Nano Energy*, 2017, **34**, 271–305.
- 10 R. Singh, P. K. Singh, B. Bhattacharya and H.-W. Rhee, *Appl. Mater. Today*, 2019, **14**, 175–200.
- 11 G. Yang, H. Tao, P. Qin, W. Ke and G. Fang, *J. Mater. Chem. A*, 2016, **4**, 3970–3990.
- 12 E. T. Hoke, D. J. Slotcavage, E. R. Dohner, A. R. Bowring, H. I. Karunadasa and M. D. McGehee, *Chem. Sci.*, 2015, **6**, 613–617.
- 13 G. Richardson, S. E. J. O’Kane, R. G. Niemann, T. A. Peltola, J. M. Foster, P. J. Cameron and A. B. Walker, *Energy Environ. Sci.*, 2016, **9**, 1476–1485.
- 14 P. Lopez-Varo, J. A. Jiménez-Tejada, M. García-Rosell, S. Ravishankar, G. Garcia-Belmonte, J. Bisquert and O. Almora, *Adv. Energy Mater.*, 2018, **8**, 1702772.
- 15 L. Bertoluzzi, C. C. Boyd, N. Rolston, J. Xu, R. Prasanna, B. C. O’Regan and M. D. McGehee, *Joule*, 2020, **4**, 109–127.
- 16 H. J. Snaith, *Nat. Mater.*, 2018, **17**, 372–376.
- 17 C. Case, N. Beaumont and D. Kirk, *ACS Energy Lett.*, 2019, **4**, 2760–2762.
- 18 A. Abate, J.-P. Correa-Baena, M. Saliba, M. S. Su’ait and F. Bella, *Chem. Eur. J.*, 2018, **24**, 3083–3100.
- 19 S. Shao and M. A. Loi, *Adv. Mater. Interfaces*, 2020, **7**, 1901469.
- 20 J. A. Christians, P. Schulz, J. S. Tinkham, T. H. Schloemer, S. P. Harvey, B. J. Tremolet de Villers, A. Sellinger, J. J. Berry and J. M. Luther, *Nat. Energy*, 2018, **3**, 68–74.
- 21 P. Zhao, B. J. Kim and H. S. Jung, *Mater. Today Energy*, 2018, **7**, 267–286.
- 22 C. C. Boyd, R. Cheacharoen, T. Leijtens and M. D. McGehee, *Chem. Rev.*, 2019, **119**, 3418–3451.
- 23 R. Wang, M. Mujahid, Y. Duan, Z. Wang, J. Xue and Y. Yang, *Adv. Funct. Mater.*, 2019, **29**, 1808843.
- 24 M. I. Asghar, J. Zhang, H. Wang and P. D. Lund, *Renew. Sustain. Energy Rev.*, 2017, **77**, 131–146.
- 25 Z. Li, T. R. Klein, D. H. Kim, M. Yang, J. J. Berry, M. F. A. M. van Hest and K. Zhu, *Nat. Rev. Mater.*, 2018, **3**, 18017.
- 26 L. Qiu, S. He, L. K. Ono, S. Liu and Y. Qi, *ACS Energy Lett.*, 2019, **4**, 2147–2167.
- 27 F. Huang, M. Li, P. Siffalovic, G. Cao and J. Tian, *Energy Environ. Sci.*, 2019, **12**, 518–549.
- 28 V. Zardetto, B. L. Williams, A. Perrotta, F. Di Giacomo, M. A. Verheijen, R. Andriessen, W. M. M. Kessels and M. Creatore, *Sustain. Energy Fuels*, 2017, **1**, 30–55.
- 29 K. O. Brinkmann, T. Gahlmann and T. Riedl, *Sol. RRL*, 2019, **4**, 1900332.
- 30 S. Seo, S. Jeong, H. Park, H. Shin and N.-G. Park, *Chem. Commun.*, 2019, **55**, 2403–2416.
- 31 P. Luo, S. Zhou, W. Xia, J. Cheng, C. Xu and Y. Lu, *Adv. Mater. Interfaces*, 2017, **4**, 1600970.
- 32 M. Meyyappan, *J. Phys. D: Appl. Phys.*, 2009, **42**, 213001.

- 33 A. Hozumi and O. Takai, *Thin Solid Films*, 1997, **303**, 222–225.
- 34 Y. Li, D. Mann, M. Rolandi, W. Kim, A. Ural, S. Hung, A. Javey, J. Cao, D. Wang, E. Yenilmez, Q. Wang, J. F. Gibbons, Y. Nishi and H. Dai, *Nano Lett.*, 2004, **4**, 317–321.
- 35 K. Haga, M. Kamidaira, Y. Kashiwaba, T. Sekiguchi and H. Watanabe, *J. Cryst. Growth*, 2000, **214**, 77–80.
- 36 C. S. Blackman, C. J. Carmalt, I. P. Parkin, L. Apostolico, K. C. Molloy, A. J. P. White and D. J. Williams, *J. Chem. Soc. Dalt. Trans.*, 2002, 2702–2709.
- 37 M. L. Hitchman and J. Kane, *J. Cryst. Growth*, 1981, **55**, 485–500.
- 38 K. C. Saraswat, D. L. Brors, J. A. Fair, K. A. Monnig and R. Beyers, *IEEE Trans. Electron Devices*, 1983, **30**, 1497–1505.
- 39 K. F. Roenigk and K. F. Jensen, *J. Electrochem. Soc.*, 1987, **134**, 1777–1785.
- 40 R. Binions, C. Piccirillo and I. P. Parkin, *Surf. Coatings Technol.*, 2007, **201**, 9369–9372.
- 41 K. Fujino, Y. Nishimoto, N. Tokumasu and K. Maeda, *J. Electrochem. Soc.*, 1990, **137**, 2883–2887.
- 42 L. S. Price, I. P. Parkin, T. G. Hibbert and K. C. Molloy, *Chem. Vap. Depos.*, 1998, **4**, 222–225.
- 43 Z. Remes, M. Vanecek, H. M. Yates, P. Evans and D. W. Sheel, *Thin Solid Films*, 2009, **517**, 6287–6289.
- 44 B. Hu, H. Ago, Y. Ito, K. Kawahara, M. Tsuji, E. Magome, K. Sumitani, N. Mizuta, K. I. Ikeda and S. Mizuno, *Carbon*, 2012, **50**, 57–65.
- 45 Y. Kashiwaba, F. Katahira, K. Haga, T. Sekiguchi and H. Watanabe, *J. Cryst. Growth*, 2000, **221**, 431–434.
- 46 P. Marchand, I. A. Hassan, I. P. Parkin and C. J. Carmalt, *Dalt. Trans.*, 2013, **42**, 9406.
- 47 H. B. Wang, C. R. Xia, G. Y. Meng and D. K. Peng, *Mater. Lett.*, 2000, **44**, 23–28.
- 48 C. Piccirillo, R. Binions and I. P. Parkin, *Chem. Vap. Depos.*, 2007, **13**, 145–151.
- 49 M. R. Waugh, G. Hyett and I. P. Parkin, *Chem. Vap. Depos.*, 2008, **14**, 366–372.
- 50 S. Vallejos, P. Umek, T. Stoycheva, F. Annanouch, E. Llobet, X. Correig, P. De Marco, C. Bittencourt and C. Blackman, *Adv. Funct. Mater.*, 2013, **23**, 1313–1322.
- 51 A. C. Jones and M. L. Hitchman, in *Chemical Vapor Deposition: Precursors, Processes and Applications*, eds. A. C. Jones and M. L. Hitchman, Royal Society of Chemistry, 2009, pp. 1–36.
- 52 V. Miikkulainen, M. Leskelä, M. Ritala and R. L. Puurunen, *J. Appl. Phys.*, 2013, **113**, 021301.
- 53 S. M. George, *Chem. Rev.*, 2010, **110**, 111–131.
- 54 R. W. Johnson, A. Hultqvist and S. F. Bent, *Mater. Today*, 2014, **17**, 236–246.
- 55 M. Knez, K. Nielsch and L. Niinistö, *Adv. Mater.*, 2007, **19**, 3425–3438.
- 56 A. S. Asundi, J. A. Raiford and S. F. Bent, *ACS Energy Lett.*, 2019, **4**, 908–925.
- 57 J. A. Singh, N. Yang and S. F. Bent, *Annu. Rev. Chem. Biomol. Eng.*, 2017, **8**, 41–62.
- 58 K. L. Nardi, N. Yang, C. F. Dickens, A. L. Strickler and S. F. Bent, *Adv. Energy Mater.*, 2015, **5**, 1500412.
- 59 B. J. O’Neill, D. H. K. Jackson, J. Lee, C. Canlas, P. C. Stair, C. L. Marshall, J. W. Elam, T. F. Kuech, J. A. Dumesic and G. W. Huber, *ACS Catal.*, 2015, **5**, 1804–1825.
- 60 Y. Wu, X. Yang, H. Chen, K. Zhang, C. Qin, J. Liu, W. Peng, A. Islam, E. Bi, F. Ye, M. Yin, P. Zhang and L. Han, *Appl. Phys. Express*, 2014, **7**, 052301.
- 61 Y. You, W. Tian, L. Min, F. Cao, K. Deng and L. Li, *Adv. Mater. Interfaces*, 2019, **7**, 1901406.
- 62 J. Zhang, Y. Chen and W. Guo, *Nano Energy*, 2018, **49**, 230–236.
- 63 A. F. Palmstrom, J. A. Raiford, R. Prasanna, K. A. Bush, M. Sponseller, R. Cheacharoen, M. C. Minichetti, D. S. Bergsman, T. Leijtens, H.-P. Wang, V. Bulović, M. D. McGehee and S. F. Bent, *Adv. Energy Mater.*, 2018, **8**, 1800591.
- 64 Q. Jiang, X. Zhang and J. You, *Small*, 2018, **14**, 1801154.
- 65 Y. Zhu, K. Deng, H. Sun, B. Gu, H. Lu, F. Cao, J. Xiong and L. Li, *Adv. Sci.*, 2018, **5**, 1700614.
- 66 Y. Lv, P. Xu, G. Ren, F. Chen, H. Nan, R. Liu, D. Wang, X. Tan, X. Liu, H. Zhang and Z.-K. Chen, *ACS Appl. Mater. Interfaces*, 2018, **10**, 23928–23937.
- 67 T. Leijtens, G. E. Eperon, S. Pathak, A. Abate, M. M. Lee and H. J. Snaith, *Nat. Commun.*, 2013,

- 4, 2885.
- 68 J. P. Correa Baena, L. Steier, W. Tress, M. Saliba, S. Neutzner, T. Matsui, F. Giordano, T. J. Jacobsson, A. R. Srimath Kandada, S. M. Zakeeruddin, A. Petrozza, A. Abate, M. K. Nazeeruddin, M. Grätzel and A. Hagfeldt, *Energy Environ. Sci.*, 2015, **8**, 2928–2934.
- 69 S. Jeong, S. Seo, H. Park and H. Shin, *Chem. Commun.*, 2019, **55**, 2433–2436.
- 70 L. Hoffmann, K. O. Brinkmann, J. Malerczyk, D. Rogalla, T. Becker, D. Theirich, I. Shutsko, P. Görrn and T. Riedl, *ACS Appl. Mater. Interfaces*, 2018, **10**, 6006–6013.
- 71 F. J. Ramos, M. C. López-Santos, E. Guillén, M. K. Nazeeruddin, M. Grätzel, A. R. Gonzalez-Elipe and S. Ahmad, *ChemPhysChem*, 2014, **15**, 1148–1153.
- 72 J. L. Hodgkinson, H. M. Yates, A. Walter, D. Sacchetto, S.-J. Moon and S. Nicolay, *J. Mater. Chem. C*, 2018, **6**, 1988–1995.
- 73 S. Chen, J. Wang, Z. Zhang, J. Briscoe, M. E. A. Warwick, H. Li and P. Hu, *Mater. Lett.*, 2018, **217**, 251–254.
- 74 B. Zhao, L. C. Lee, L. Yang, A. J. Pearson, H. Lu, X.-J. She, L. Cui, K. H. L. Zhang, R. L. Z. Hoye, A. Karani, P. Xu, A. Sadhanala, N. C. Greenham, R. H. Friend, J. L. MacManus-Driscoll and D. Di, *ACS Appl. Mater. Interfaces*, 2018, **10**, 41849–41854.
- 75 D. Koushik, M. Jošt, A. Dučinskas, C. Burgess, V. Zardetto, C. Weijtens, M. A. Verheijen, W. M. M. Kessels, S. Albrecht and M. Creatore, *J. Mater. Chem. C*, 2019, **7**, 12532–12543.
- 76 Z. Zhu, Y. Bai, T. Zhang, Z. Liu, X. Long, Z. Wei, Z. Wang, L. Zhang, J. Wang, F. Yan and S. Yang, *Angew. Chemie*, 2014, **126**, 12779–12783.
- 77 S. Seo, I. J. Park, M. Kim, S. Lee, C. Bae, H. S. Jung, N.-G. G. Park, J. Y. Kim and H. Shin, *Nanoscale*, 2016, **8**, 11403–11412.
- 78 S. Chu, R. Zhao, R. Liu, Y. Gao, X. Wang, C. Liu, J. Chen and H. Zhou, *Semicond. Sci. Technol.*, 2018, **33**, 115016.
- 79 J. A. Raiford, R. A. Belisle, K. A. Bush, R. Prasanna, A. F. Palmstrom, M. D. McGehee and S. F. Bent, *Sustain. Energy Fuels*, 2019, **3**, 1517–1525.
- 80 W. Tan, O. L. Hendricks, A. C. Meng, M. R. Braun, M. D. McGehee, C. E. D. Chidsey and P. C. McIntyre, *Adv. Mater. Interfaces*, 2018, **5**, 1800191.
- 81 Y. G. Kim, K. C. Kwon, Q. Van Le, K. Hong, H. W. Jang and S. Y. Kim, *J. Power Sources*, 2016, **319**, 1–8.
- 82 B. Cao, L. Yang, S. Jiang, H. Lin, N. Wang and X. Li, *J. Mater. Chem. A*, 2019, **7**, 4960–4970.
- 83 Y. H. Lee, J. Luo, M.-K. Son, P. Gao, K. T. Cho, J. Seo, S. M. Zakeeruddin, M. Grätzel and M. K. Nazeeruddin, *Adv. Mater.*, 2016, **28**, 3966–3972.
- 84 P. Poodt, A. Lankhorst, F. Roozeboom, K. Spee, D. Maas and A. Vermeer, *Adv. Mater.*, 2010, **22**, 3564–3567.
- 85 S. Li, P. Zhang, Y. Wang, H. Sarvari, D. Liu, J. Wu, Y. Yang, Z. Wang and Z. D. Chen, *Nano Res.*, 2017, **10**, 1092–1103.
- 86 D. Koushik, W. J. H. Verhees, D. Zhang, Y. Kuang, S. Veenstra, M. Creatore and R. E. I. Schropp, *Adv. Mater. Interfaces*, 2017, **4**, 1700043.
- 87 I. S. Kim and A. B. F. Martinson, *J. Mater. Chem. A*, 2015, **3**, 20092–20096.
- 88 H. Si, Q. Liao, Z. Zhang, Y. Li, X. Yang, G. Zhang, Z. Kang and Y. Zhang, *Nano Energy*, 2016, **22**, 223–231.
- 89 D. Koushik, W. J. H. Verhees, Y. Kuang, S. Veenstra, D. Zhang, M. A. Verheijen, M. Creatore and R. E. I. Schropp, *Energy Environ. Sci.*, 2017, **10**, 91–100.
- 90 M. Jaysankar, B. A. L. Raul, J. Bastos, C. Burgess, C. Weijtens, M. Creatore, T. Aernouts, Y. Kuang, R. Gehlhaar, A. Hadipour and J. Poortmans, *ACS Energy Lett.*, 2019, **4**, 259–264.
- 91 R. D. Chavan, M. M. Tavakoli, D. Prochowicz, P. Yadav, S. S. Lote, S. P. Bhoite, A. Nimbalkar and C. K. Hong, *ACS Appl. Mater. Interfaces*, 2020, **12**, 8098–8106.
- 92 X. Hu, X.-F. Jiang, X. Xing, L. Nian, X. Liu, R. Huang, K. Wang, H.-L. Yip and G. Zhou, *Sol. RRL*, 2018, **2**, 1800083.
- 93 S. S. Mali, C. S. Shim, H. K. Park, J. Heo, P. S. Patil and C. K. Hong, *Chem. Mater.*, 2015, **27**,

- 1541–1551.
- 94 S. Ray, R. Banerjee, N. Basu, A. K. Batabyal and A. K. Barua, *J. Appl. Phys.*, 1983, **54**, 3497–3501.
- 95 D. S. Hecht, L. Hu and G. Irvin, *Adv. Mater.*, 2011, **23**, 1482–1513.
- 96 J. Yoon, H. Sung, G. Lee, W. Cho, N. Ahn, H. S. Jung and M. Choi, *Energy Environ. Sci.*, 2017, **10**, 337–345.
- 97 H. Sung, N. Ahn, M. S. Jang, J. K. Lee, H. Yoon, N. G. Park and M. Choi, *Adv. Energy Mater.*, 2016, **6**, 2–7.
- 98 Q. Luo, H. Ma, Q. Hou, Y. Li, J. Ren, X. Dai, Z. Yao, Y. Zhou, L. Xiang, H. Du, H. He, N. Wang, K. Jiang, H. Lin, H. Zhang and Z. Guo, *Adv. Funct. Mater.*, 2018, **28**, 1706777.
- 99 X. Li, Y. Zhu, W. Cai, M. Borysiak, B. Han, D. Chen, R. D. Piner, L. Colomba and R. S. Ruoff, *Nano Lett.*, 2009, **9**, 4359–4363.
- 100 W. H. Lee, J. Park, S. H. Sim, S. B. Jo, K. S. Kim, B. H. Hong and K. Cho, *Adv. Mater.*, 2011, **23**, 1752–1756.
- 101 M. M. Tavakoli, M. Nasilowski, J. Zhao, M. G. Bawendi and J. Kong, *Small Methods*, 2019, **3**, 1900449.
- 102 P. You, Z. Liu, Q. Tai, S. Liu and F. Yan, *Adv. Mater.*, 2015, **27**, 3632–3638.
- 103 S. Kim, S. H. Shin and S. H. Choi, *J. Alloys Compd.*, 2019, **786**, 614–620.
- 104 H. Li, K. Cao, J. Cui, S. Liu, X. Qiao, Y. Shen and M. Wang, *Nanoscale*, 2016, **8**, 6379–6385.
- 105 T. P. Tyler, R. E. Brock, H. J. Karmel, T. J. Marks and M. C. Hersam, *Adv. Energy Mater.*, 2011, **1**, 785–791.
- 106 I. Jeon, S. Seo, Y. Sato, C. Delacou, A. Anisimov, K. Suenaga, E. I. Kauppinen, S. Maruyama and Y. Matsuo, *J. Phys. Chem. C*, 2017, **121**, 25743–25749.
- 107 G. E. Eperon, V. M. Burlakov, P. Docampo, A. Goriely and H. J. Snaith, *Adv. Funct. Mater.*, 2014, **24**, 151–157.
- 108 D. H. Kim, J. B. Whitaker, Z. Li, M. F. A. M. van Hest and K. Zhu, *Joule*, 2018, **2**, 1437–1451.
- 109 A. Babayigit, A. Ethirajan, M. Muller and B. Conings, *Nat. Mater.*, 2016, **15**, 247–251.
- 110 Y. Deng, E. Peng, Y. Shao, Z. Xiao, Q. Dong and J. Huang, *Energy Environ. Sci.*, 2015, **8**, 1544–1550.
- 111 C. Tian, F. Wang, Y. Wang, Z. Yang, X. Chen, J. Mei, H. Liu and D. Zhao, *ACS Appl. Mater. Interfaces*, 2019, **11**, 15804–15812.
- 112 P. Luo, Z. Liu, W. Xia, C. Yuan, J. Cheng and Y. Lu, *J. Mater. Chem. A*, 2015, **3**, 12443–12451.
- 113 S. Basak, M. Afzaal and H. M. Yates, *Mater. Chem. Phys.*, 2019, **223**, 157–163.
- 114 M. R. Leyden, L. K. Ono, S. R. Raga, Y. Kato, S. Wang and Y. Qi, *J. Mater. Chem. A*, 2014, **2**, 18742–18745.
- 115 C. Surya, G. Li, A. B. Djurišić, A. Ng and Z. Ren, in *Oxide-based Materials and Devices IX*, eds. F. H. Teherani, D. C. Look and D. J. Rogers, SPIE, 2018, vol. 10533.
- 116 X. Wei, Y. Peng, G. Jing and T. Cui, *Jpn. J. Appl. Phys.*, 2018, **57**, 052301.
- 117 M. M. Tavakoli, S. M. Zakeeruddin, M. Grätzel and Z. Fan, *Adv. Mater.*, 2018, **30**, 1705998.
- 118 M. M. Tavakoli, L. Gu, Y. Gao, C. Reckmeier, J. He, A. L. Rogach, Y. Yao and Z. Fan, *Sci. Rep.*, 2015, **5**, 14083.
- 119 D. J. Lewis and P. O’Brien, *Chem. Commun.*, 2014, **50**, 6319–6321.
- 120 D. S. Bhachu, D. O. Scanlon, E. J. Saban, H. Bronstein, I. P. Parkin, C. J. Carmalt and R. G. Palgrave, *J. Mater. Chem. A*, 2015, **3**, 9071–9073.
- 121 M. Afzaal and H. M. Yates, *Surf. Coatings Technol.*, 2017, **321**, 336–340.
- 122 B. R. Sutherland, S. Hoogland, M. M. Adachi, P. Kanjanaboos, C. T. O. Wong, J. J. McDowell, J. Xu, O. Voznyy, Z. Ning, A. J. Houtepen and E. H. Sargent, *Adv. Mater.*, 2015, **27**, 53–58.
- 123 J. Ávila, C. Momblona, P. P. Boix, M. Sessolo and H. J. Bolink, *Joule*, 2017, **1**, 431–442.
- 124 L. K. Ono, M. R. Leyden, S. Wang and Y. Qi, *J. Mater. Chem. A*, 2016, **4**, 6693–6713.
- 125 M. Liu, M. B. Johnston and H. J. Snaith, *Nature*, 2013, **501**, 395–398.
- 126 O. Malinkiewicz, A. Yella, Y. H. Lee, G. M. Espallargas, M. Graetzel, M. K. Nazeeruddin and H.

- J. Bolink, *Nat. Photonics*, 2014, **8**, 128–132.
- 127 S. Wang, L. K. Ono, M. R. Leyden, Y. Kato, S. R. Raga, M. V. Lee and Y. Qi, *J. Mater. Chem. A*, 2015, **3**, 14631–14641.
- 128 A. F. Palmstrom, G. E. Eperon, T. Leijtens, R. Prasanna, S. N. Habisreutinger, W. Nemeth, E. A. Gaulding, S. P. Dunfield, M. Reese, S. Nanayakkara, T. Moot, J. Werner, J. Liu, B. To, S. T. Christensen, M. D. McGehee, M. F. A. M. van Hest, J. M. Luther, J. J. Berry and D. T. Moore, *Joule*, 2019, **3**, 2193–2204.
- 129 J. Xu, C. C. Boyd, Z. J. Yu, A. F. Palmstrom, D. J. Witter, B. W. Larson, R. M. France, J. Werner, S. P. Harvey, E. J. Wolf, W. Weigand, S. Manzoor, M. F. A. M. van Hest, J. J. Berry, J. M. Luther, Z. C. Holman and M. D. McGehee, *Science*, 2020, **367**, 1097–1104.
- 130 H. Hu, D. Wang, Y. Zhou, J. Zhang, S. Lv, S. Pang, X. Chen, Z. Liu, N. P. Padture and G. Cui, *RSC Adv.*, 2014, **4**, 28964–28967.
- 131 Y. Zhou, M. Yang, S. Pang, K. Zhu and N. P. Padture, *J. Am. Chem. Soc.*, 2016, **138**, 5535–5538.
- 132 P. Fan, D. Gu, G. X. Liang, J. T. Luo, J. L. Chen, Z. H. Zheng and D. P. Zhang, *Sci. Rep.*, 2016, **6**, 1–9.
- 133 G. Longo, L. Gil-Escrig, M. J. Degen, M. Sessolo and H. J. Bolink, *Chem. Commun.*, 2015, **51**, 7376–7378.
- 134 A. De Vos, *J. Phys. D: Appl. Phys.*, 1980, **13**, 839–846.
- 135 T. Leijtens, K. A. Bush, R. Prasanna and M. D. McGehee, *Nat. Energy*, 2018, **3**, 828–838.
- 136 R. Prasanna, A. Gold-Parker, T. Leijtens, B. Conings, A. Babayigit, H.-G. Boyen, M. F. Toney and M. D. McGehee, *J. Am. Chem. Soc.*, 2017, **139**, 11117–11124.
- 137 G. E. Eperon, M. T. Hörantner and H. J. Snaith, *Nat. Rev. Chem.*, 2017, **1**, 0095.
- 138 B. Chen, X. Zheng, Y. Bai, N. P. Padture and J. Huang, *Adv. Energy Mater.*, 2017, **7**, 1602400.
- 139 J. Werner, B. Niesen and C. Ballif, *Adv. Mater. Interfaces*, 2018, **5**, 1700731.
- 140 K. A. Bush, A. F. Palmstrom, Z. J. Yu, M. Boccard, R. Checharoen, J. P. Mailoa, D. P. McMeekin, R. L. Z. Hoye, C. D. Bailie, T. Leijtens, I. M. Peters, M. C. Minichetti, N. Rolston, R. Prasanna, S. Sofia, D. Harwood, W. Ma, F. Moghadam, H. J. Snaith, T. Buonassisi, Z. C. Holman, S. F. Bent and M. D. McGehee, *Nat. Energy*, 2017, **2**, 17009.
- 141 K. A. Bush, S. Manzoor, K. Frohna, Z. J. Yu, J. A. Raiford, A. F. Palmstrom, H.-P. Wang, R. Prasanna, S. F. Bent, Z. C. Holman and M. D. McGehee, *ACS Energy Lett.*, 2018, **3**, 2173–2180.
- 142 B. Chen, Z. Yu, K. Liu, X. Zheng, Y. Liu, J. Shi, D. Spronk, P. N. Rudd, Z. Holman and J. Huang, *Joule*, 2019, **3**, 177–190.
- 143 M. Jošt, E. Köhnen, A. B. Morales-Vilches, B. Lipovšek, K. Jäger, B. Macco, A. Al-Ashouri, J. Krč, L. Korte, B. Rech, R. Schlattmann, M. Topič, B. Stannowski and S. Albrecht, *Energy Environ. Sci.*, 2018, **11**, 3511–3523.
- 144 F. Sahli, J. Werner, B. A. Kamino, M. Bräuninger, R. Monnard, B. Paviet-Salomon, L. Barraud, L. Ding, J. J. Diaz Leon, D. Sacchetto, G. Cattaneo, M. Despeisse, M. Boccard, S. Nicolay, Q. Jeangros, B. Niesen and C. Ballif, *Nat. Mater.*, 2018, **17**, 820–826.
- 145 J. Zheng, H. Mehrvarz, C. Liao, J. Bing, X. Cui, Y. Li, V. R. Gonçalves, C. F. J. Lau, D. S. Lee, Y. Li, M. Zhang, J. Kim, Y. Cho, L. G. Caro, S. Tang, C. Chen, S. Huang and A. W. Y. Ho-Baillie, *ACS Energy Lett.*, 2019, **4**, 2623–2631.
- 146 H. Shen, S. T. Omelchenko, D. A. Jacobs, S. Yalamanchili, Y. Wan, D. Yan, P. Phang, T. Duong, Y. Wu, Y. Yin, C. Samundsett, J. Peng, N. Wu, T. P. White, G. G. Andersson, N. S. Lewis and K. R. Catchpole, *Sci. Adv.*, 2018, **4**, eaau9711.
- 147 J. Werner, C.-H. Weng, A. Walter, L. Fesquet, J. P. Seif, S. De Wolf, B. Niesen and C. Ballif, *J. Phys. Chem. Lett.*, 2016, **7**, 161–166.
- 148 M. Jošt, T. Bertram, D. Koushik, J. A. Marquez, M. A. Verheijen, M. D. Heinemann, E. Köhnen, A. Al-Ashouri, S. Braunger, F. Lang, B. Rech, T. Unold, M. Creatore, I. Laueremann, C. A. Kaufmann, R. Schlattmann and S. Albrecht, *ACS Energy Lett.*, 2019, **4**, 583–590.
- 149 G. E. Eperon, T. Leijtens, K. A. Bush, R. Prasanna, T. Green, J. T.-W. Wang, D. P. McMeekin, G. Volonakis, R. L. Milot, R. May, A. Palmstrom, D. J. Slotcavage, R. A. Belisle, J. B. Patel, E. S.

- Parrott, R. J. Sutton, W. Ma, F. Moghadam, B. Conings, A. Babayigit, H.-G. Boyen, S. Bent, F. Giustino, L. M. Herz, M. B. Johnston, M. D. McGehee and H. J. Snaith, *Science*, 2016, **354**, 861–865.
- 150 J. Tong, Z. Song, D. H. Kim, X. Chen, C. Chen, A. F. Palmstrom, P. F. Ndione, M. O. Reese, S. P. Dunfield, O. G. Reid, J. Liu, F. Zhang, S. P. Harvey, Z. Li, S. T. Christensen, G. Teeter, D. Zhao, M. M. Al-Jassim, M. F. A. M. van Hest, M. C. Beard, S. E. Shaheen, J. J. Berry, Y. Yan and K. Zhu, *Science*, 2019, **364**, 475–479.
- 151 D. Zhao, Y. Yu, C. Wang, W. Liao, N. Shrestha, C. R. Grice, A. J. Cimaroli, L. Guan, R. J. Ellingson, K. Zhu, X. Zhao, R.-G. Xiong and Y. Yan, *Nat. Energy*, 2017, **2**, 17018.
- 152 D. Zhao, C. Wang, Z. Song, Y. Yu, C. Chen, X. Zhao, K. Zhu and Y. Yan, *ACS Energy Lett.*, 2018, **3**, 305–306.
- 153 R. Lin, K. Xiao, Z. Qin, Q. Han, C. Zhang, M. Wei, M. I. Saidaminov, Y. Gao, J. Xu, M. Xiao, A. Li, J. Zhu, E. H. Sargent and H. Tan, *Nat. Energy*, 2019, **4**, 864–873.
- 154 D. H. Kim, C. P. Muzzillo, J. Tong, A. F. Palmstrom, B. W. Larson, C. Choi, S. P. Harvey, S. Glynn, J. B. Whitaker, F. Zhang, Z. Li, H. Lu, M. F. A. M. van Hest, J. J. Berry, L. M. Mansfield, Y. Huang, Y. Yan and K. Zhu, *Joule*, 2019, **3**, 1734–1745.
- 155 G. Nogay, F. Sahli, J. Werner, R. Monnard, M. Boccard, M. Despeisse, F.-J. Haug, Q. Jeangros, A. Ingenito and C. Ballif, *ACS Energy Lett.*, 2019, **4**, 844–845.
- 156 E. M. Sanehira, B. J. Tremolet de Villers, P. Schulz, M. O. Reese, S. Ferrere, K. Zhu, L. Y. Lin, J. J. Berry and J. M. Luther, *ACS Energy Lett.*, 2016, **1**, 38–45.
- 157 P. Schulz, J. O. Tjepelt, J. A. Christians, I. Levine, E. Edri, E. M. Sanehira, G. Hodes, D. Cahen and A. Kahn, *ACS Appl. Mater. Interfaces*, 2016, **8**, 31491–31499.
- 158 S. Albrecht, M. Saliba, J. P. Correa Baena, F. Lang, L. Kegelmann, M. Mews, L. Steier, A. Abate, J. Rappich, L. Korte, R. Schlattmann, M. K. Nazeeruddin, A. Hagfeldt, M. Grätzel and B. Rech, *Energy Environ. Sci.*, 2016, **9**, 81–88.
- 159 J. P. Mailoa, C. D. Bailie, E. C. Johlin, E. T. Hoke, A. J. Akey, W. H. Nguyen, M. D. McGehee and T. Buonassisi, *Appl. Phys. Lett.*, 2015, **106**, 121105.
- 160 F. Sahli, B. A. Kamino, J. Werner, M. Bräuninger, B. Paviet-Salomon, L. Barraud, R. Monnard, J. P. Seif, A. Tomasi, Q. Jeangros, A. Hessler-Wyser, S. De Wolf, M. Despeisse, S. Nicolay, B. Niesen and C. Ballif, *Adv. Energy Mater.*, 2018, **8**, 1701609.
- 161 D. Yu, Y.-Q. Yang, Z. Chen, Y. Tao and Y.-F. Liu, *Opt. Commun.*, 2016, **362**, 43–49.
- 162 E. Y. Choi, J. Kim, S. Lim, E. Han, A. W. Y. Ho-Baillie and N. Park, *Sol. Energy Mater. Sol. Cells*, 2018, **188**, 37–45.
- 163 F. J. Ramos, T. Maindron, S. Béchu, A. Rebai, M. Frégnaux, M. Bouttemy, J. Rousset, P. Schulz and N. Schneider, *Sustain. Energy Fuels*, 2018, **2**, 2468–2479.
- 164 C.-Y. Chang, K.-T. Lee, W.-K. Huang, H.-Y. Siao and Y.-C. Chang, *Chem. Mater.*, 2015, **27**, 5122–5130.
- 165 E. Y. Choi, J.-H. Kim, B.-J. Kim, J. H. Jang, J. Kim and N. Park, *RSC Adv.*, 2019, **9**, 11737–11744.
- 166 Y. Il Lee, N. J. Jeon, B. J. Kim, H. Shim, T.-Y. Yang, S. Il Seok, J. Seo and S. G. Im, *Adv. Energy Mater.*, 2018, **8**, 1701928.
- 167 H. Wang, Y. Zhao, Z. Wang, Y. Liu, Z. Zhao, G. Xu, T.-H. Han, J.-W. Lee, C. Chen, D. Bao, Y. Huang, Y. Duan and Y. Yang, *Nano Energy*, 2020, **69**, 104275.
- 168 X. Dong, X. Fang, M. Lv, B. Lin, S. Zhang, J. Ding and N. Yuan, *J. Mater. Chem. A*, 2015, **3**, 5360–5367.
- 169 M. Kot, C. Das, Z. Wang, K. Henkel, Z. Rouissi, K. Wojciechowski, H. J. Snaith and D. Schmeisser, *ChemSusChem*, 2016, **9**, 3401–3406.
- 170 D. Koushik, F. Naziris, J. Melskens, A. Nusteling, V. Zardetto, H. Schut, W. M. M. Kessels, S. W. H. Eijt and M. Creatore, *J. Mater. Chem. C*, 2019, **7**, 5275–5284.
- 171 H. Wei, J. Shi, X. Xu, J. Xiao, J. Luo, J. Dong, S. Lv, L. Zhu, H. Wu, D. Li, Y. Luo, Q. Meng and Q. Chen, *Phys. Chem. Chem. Phys.*, 2015, **17**, 4937–4944.

- 172 J.-J. Shi, W. Dong, Y.-Z. Xu, C.-H. Li, S.-T. Lv, L.-F. Zhu, J. Dong, Y.-H. Luo, D.-M. Li, Q.-B. Meng and Q. Chen, *Chinese Phys. Lett.*, 2013, **30**, 128402.
- 173 D. Koushik, L. Hazendonk, V. Zardetto, V. Vandalon, M. A. Verheijen, W. M. M. Kessels and M. Creatore, *ACS Appl. Mater. Interfaces*, 2019, **11**, 5526–5535.
- 174 D. Choudhury, G. Rajaraman and S. K. Sarkar, *Nanoscale*, 2016, **8**, 7459–7465.
- 175 X. Yu, H. Yan and Q. Peng, *Langmuir*, 2019, **35**, 6522–6531.
- 176 A. Hultqvist, K. Aitola, K. Sveinbjörnsson, Z. Saki, F. Larsson, T. Törndahl, E. Johansson, G. Boschloo and M. Edoff, *ACS Appl. Mater. Interfaces*, 2017, **9**, 29707–29716.
- 177 M. Kot, L. Kegelmann, C. Das, P. Kus, N. Tsud, I. Matolinova, S. Albrecht, V. Matolin and D. Schmeisser, *ChemSusChem*, 2018, **11**, 3640–3648.
- 178 J. Zhang, A. Hultqvist, T. Zhang, L. Jiang, C. Ruan, L. Yang, Y. Cheng, M. Edoff and E. M. J. Johansson, *ChemSusChem*, 2017, **10**, 3810–3817.
- 179 S. Seo, S. Jeong, C. Bae, N.-G. Park and H. Shin, *Adv. Mater.*, 2018, **30**, 1801010.
- 180 H. Wei, J. Wu, P. Qiu, S. Liu, Y. He, M. Peng, D. Li, Q. Meng, F. Zaera and X. Zheng, *J. Mater. Chem. A*, 2019, **7**, 25347–25354.
- 181 J. Ma, M. Zheng, C. Chen, Z. Zhu, X. Zheng, Z. Chen, Y. Guo, C. Liu, Y. Yan and G. Fang, *Adv. Funct. Mater.*, 2018, **28**, 1804128.
- 182 G. Popov, M. Mattinen, T. Hatanpää, M. Vehkamäki, M. Kemell, K. Mizohata, J. Räisänen, M. Ritala and M. Leskelä, *Chem. Mater.*, 2019, **31**, 1101–1109.
- 183 K. O. Brinkmann, J. Zhao, N. Pourdavoud, T. Becker, T. Hu, S. Olthof, K. Meerholz, L. Hoffmann, T. Gahlmann, R. Heiderhoff, M. F. Oszejca, N. A. Luechinger, D. Rogalla, Y. Chen, B. Cheng and T. Riedl, *Nat. Commun.*, 2017, **8**, 13938.
- 184 J. Zhao, K. O. Brinkmann, T. Hu, N. Pourdavoud, T. Becker, T. Gahlmann, R. Heiderhoff, A. Polywka, P. Görrn, Y. Chen, B. Cheng and T. Riedl, *Adv. Energy Mater.*, 2017, **7**, 1602599.
- 185 M. M. McCarthy, A. Walter, S.-J. Moon, N. K. Noel, S. O'Brien, M. E. Pemble, S. Nicolay, B. Wenger, H. J. Snaitth and I. M. Povey, *MRS Adv.*, 2018, **3**, 3075–3084.
- 186 Y. Kuang, V. Zardetto, R. van Gils, S. Karwal, D. Koushik, M. A. Verheijen, L. E. Black, C. Weijtens, S. Veenstra, R. Andriessen, W. M. M. Kessels and M. Creatore, *ACS Appl. Mater. Interfaces*, 2018, **10**, 30367–30378.
- 187 C. Wang, L. Guan, D. Zhao, Y. Yu, C. R. Grice, Z. Song, R. A. Awni, J. Chen, J. Wang, X. Zhao and Y. Yan, *ACS Energy Lett.*, 2017, **2**, 2118–2124.
- 188 C. Wang, D. Zhao, C. R. Grice, W. Liao, Y. Yu, A. Cimaroli, N. Shrestha, P. J. Roland, J. Chen, Z. Yu, P. Liu, N. Cheng, R. J. Ellingson, X. Zhao and Y. Yan, *J. Mater. Chem. A*, 2016, **4**, 12080–12087.
- 189 C. Wang, C. Xiao, Y. Yu, D. Zhao, R. A. Awni, C. R. Grice, K. Ghimire, I. Constantinou, W. Liao, A. J. Cimaroli, P. Liu, J. Chen, N. J. Podraza, C.-S. Jiang, M. M. Al-Jassim, X. Zhao and Y. Yan, *Adv. Energy Mater.*, 2017, **7**, 1700414.
- 190 Y. Lee, S. Lee, G. Seo, S. Paek, K. T. Cho, A. J. Huckaba, M. Calizzi, D. Choi, J.-S. Park, D. Lee, H. J. Lee, A. M. Asiri and M. K. Nazeeruddin, *Adv. Sci.*, 2018, **5**, 1800130.
- 191 J.-P. Correa-Baena, W. Tress, K. Domanski, E. H. Anaraki, S.-H. Turren-Cruz, B. Roose, P. P. Boix, M. Grätzel, M. Saliba, A. Abate and A. Hagfeldt, *Energy Environ. Sci.*, 2017, **10**, 1207–1212.
- 192 R. B. M. Hill, S.-H. Turren-Cruz, F. Pulvirenti, W. R. Tress, S. Wiegold, S. Sun, L. Nienhaus, M. Bawendi, T. Buonassisi, S. Barlow, A. Hagfeldt, S. R. Marder and J.-P. Correa-Baena, *ACS Appl. Energy Mater.*, 2019, **2**, 2402–2408.
- 193 T. Hu, T. Becker, N. Pourdavoud, J. Zhao, K. O. Brinkmann, R. Heiderhoff, T. Gahlmann, Z. Huang, S. Olthof, K. Meerholz, D. Töbrens, B. Cheng, Y. Chen and T. Riedl, *Adv. Mater.*, 2017, **29**, 1606656.
- 194 J. A. Raiford, C. C. Boyd, A. F. Palmstrom, E. J. Wolf, B. A. Fearon, J. J. Berry, M. D. McGehee and S. F. Bent, *Adv. Energy Mater.*, 2019, **9**, 1902353.
- 195 C. C. Boyd, R. Checharoen, K. A. Bush, R. Prasanna, T. Leijtens and M. D. McGehee, *ACS*

- Energy Lett.*, 2018, **3**, 1772–1778.
- 196 T. Leijtens, R. Prasanna, K. A. Bush, G. E. Eperon, J. A. Raiford, A. Gold-Parker, E. J. Wolf, S. A. Swifter, C. C. Boyd, H.-P. Wang, M. F. Toney, S. F. Bent and M. D. McGehee, *Sustain. Energy Fuels*, 2018, **2**, 2450–2459.
- 197 K. E. Roelofs, V. L. Pool, D. A. Bobb-Semple, A. F. Palmstrom, P. K. Santra, D. G. Van Campen, M. F. Toney and S. F. Bent, *Adv. Mater. Interfaces*, 2016, **3**, 1600580.
- 198 W. Li, H. Dong, X. Guo, N. Li, J. Li, G. Niu and L. Wang, *J. Mater. Chem. A*, 2014, **2**, 20105–20111.
- 199 S. Na, S. Lee, W.-G. Choi, C.-G. Park, S. O. Ryu and T. Moon, *J. Vac. Sci. Technol. A*, 2019, **37**, 010902.
- 200 A. E. Shalan, S. Narra, T. Oshikiri, K. Ueno, X. Shi, H.-P. Wu, M. M. Elshanawany, E. Wei-Guang Diao and H. Misawa, *Sustain. Energy Fuels*, 2017, **1**, 1533–1540.
- 201 L. Chen, J.-R. Wang, L.-Q. Xie, C. Zhan, Z. Qiu, J.-Z. Zhou, J.-W. Yan, B.-W. Mao and Z.-Q. Tian, *Electrochem. Commun.*, 2016, **68**, 40–44.
- 202 T.-Y. Jin, W. Li, Y.-Q. Li, Y.-X. Luo, Y. Shen, L.-P. Cheng and J.-X. Tang, *Adv. Opt. Mater.*, 2018, **6**, 1801153.
- 203 F. Di Giacomo, V. Zardetto, A. D’Epifanio, S. Pescetelli, F. Matteocci, S. Razza, A. Di Carlo, S. Licoccia, W. M. M. Kessels, M. Creatore and T. M. Brown, *Adv. Energy Mater.*, 2015, **5**, 1401808.
- 204 F. Di Giacomo, V. Zardetto, G. Lucarelli, L. Cinà, A. Di Carlo, M. Creatore and T. M. Brown, *Nano Energy*, 2016, **30**, 460–469.
- 205 V. Zardetto, F. Di Giacomo, G. Lucarelli, W. M. M. Kessels, T. M. Brown and M. Creatore, *Sol. Energy*, 2017, **150**, 447–453.
- 206 H. Zhang, H. Liu, W. Lu, W. Zhang, Y. Hao, P. Wang and W. Yu, *Mater. Lett.*, 2019, **236**, 736–738.
- 207 H. Lu, K. Deng, N. Yan, Y. Ma, B. Gu, Y. Wang and L. Li, *Sci. Bull.*, 2016, **61**, 778–786.
- 208 H. Lu, Y. Ma, B. Gu, W. Tian and L. Li, *J. Mater. Chem. A*, 2015, **3**, 16445–16452.
- 209 I. S. Kim, D. H. Cao, D. B. Buchholz, J. D. Emery, O. K. Farha, J. T. Hupp, M. G. Kanatzidis and A. B. F. Martinson, *Nano Lett.*, 2016, **16**, 7786–7790.
- 210 W. Zhu, W. Chai, Z. Zhang, D. Chen, J. Chang, S. Liu, J. Zhang, C. Zhang and Y. Hao, *Org. Electron.*, 2019, **74**, 103–109.
- 211 A. K. Chandiran, A. Yella, M. T. Mayer, P. Gao, M. K. Nazeeruddin and M. Grätzel, *Adv. Mater.*, 2014, **26**, 4309–4312.
- 212 D. Chen, A. Su, X. Li, S. Pang, W. Zhu, H. Xi, J. Chang, J. Zhang, C. Zhang and Y. Hao, *Sol. Energy*, 2019, **188**, 239–246.
- 213 H. Lu, W. Tian, B. Gu, Y. Zhu and L. Li, *Small*, 2017, **13**, 1701535.
- 214 T. W. Kim, S. Uchida, T. Kondo and H. Segawa, *Appl. Phys. Lett.*, 2019, **115**, 203902.
- 215 H. Sun, K. Deng, Y. Zhu, M. Liao, J. Xiong, Y. Li and L. Li, *Adv. Mater.*, 2018, **30**, 1801935.
- 216 H. Hu, B. Dong, H. Hu, F. Chen, M. Kong, Q. Zhang, T. Luo, L. Zhao, Z. Guo, J. Li, Z. Xu, S. Wang, D. Eder and L. Wan, *ACS Appl. Mater. Interfaces*, 2016, **8**, 17999–18007.
- 217 F. Hao, C. C. Stoumpos, D. H. Cao, R. P. H. Chang and M. G. Kanatzidis, *Nat. Photonics*, 2014, **8**, 489–494.
- 218 B. J. Kim, D. H. Kim, Y.-Y. Lee, H.-W. Shin, G. S. Han, J. S. Hong, K. Mahmood, T. K. Ahn, Y.-C. Joo, K. S. Hong, N.-G. Park, S. Lee and H. S. Jung, *Energy Environ. Sci.*, 2015, **8**, 916–921.
- 219 V. Zardetto, F. di Giacomo, H. Lifka, M. A. Verheijen, C. H. L. Weijtens, L. E. Black, S. Veenstra, W. M. M. Kessels, R. Andriessen and M. Creatore, *Adv. Mater. Interfaces*, 2018, **5**, 1701456.
- 220 J. Dong, X. Xu, J.-J. Shi, D.-M. Li, Y.-H. Luo, Q.-B. Meng and Q. Chen, *Chinese Phys. Lett.*, 2015, **32**, 78401.
- 221 X. Dong, H. Hu, B. Lin, J. Ding and N. Yuan, *Chem. Commun.*, 2014, **50**, 14405–14408.
- 222 M. Najafī, V. Zardetto, D. Zhang, D. Koushik, M. S. Dörenkämper, M. Creatore, R. Andriessen, P.

- Poodt and S. Veenstra, *Sol. RRL*, 2018, **2**, 1800147.
- 223 A. K. Chandiran, M. Abdi-Jalebi, A. Yella, M. I. Dar, C. Yi, S. A. Shivashankar, M. K. Nazeeruddin and M. Grätzel, *Nano Lett.*, 2014, **14**, 1190–1195.
- 224 R. D. Chavan, P. Yadav, M. M. Tavakoli, D. Prochowicz, A. Nimbalkar, S. P. Bhoite, P. N. Bhosale and C. K. Hong, *Sustain. Energy Fuels*, 2020, **4**, 843–851.
- 225 R. Singh, S. Ghosh, A. S. Subbiah, N. Mahuli and S. K. Sarkar, *Sol. Energy Mater. Sol. Cells*, 2020, **205**, 110289.